1259

L3P

Lepton and Photon Precision Physics

Superconducting
Coil

CeF$_3$ Crystals

Tracker

Outer Muon Detector

Part of the L3 Magnet

μ Muon Chamber

Hadron Calorimeter

L3 Forward
Muon System

8   4   6
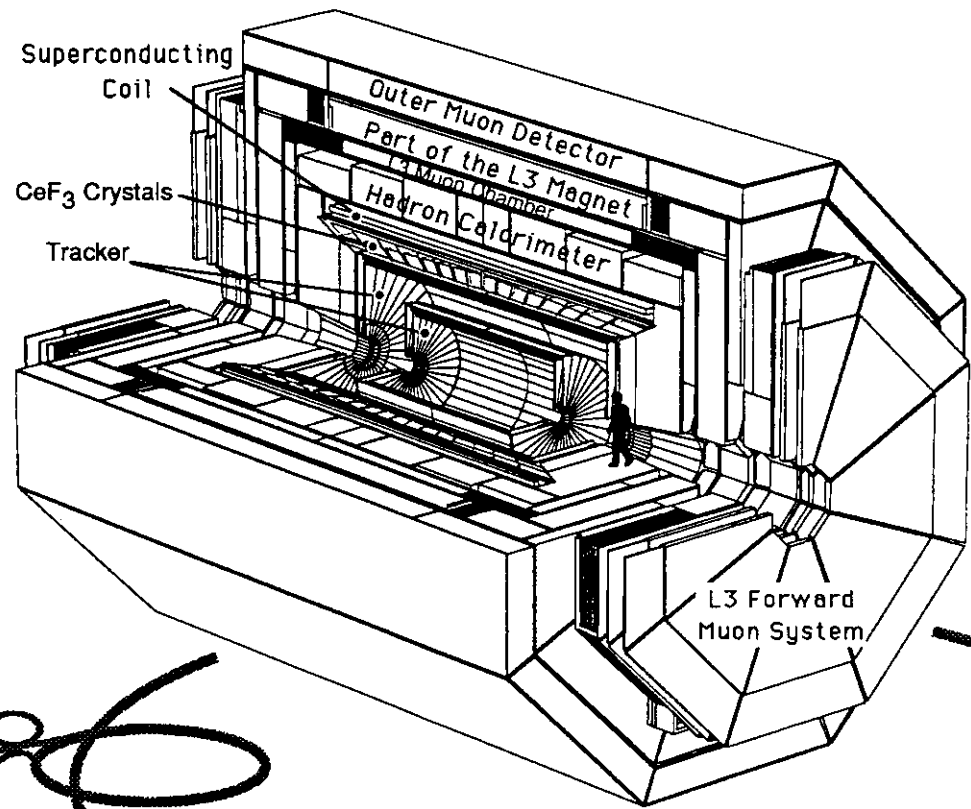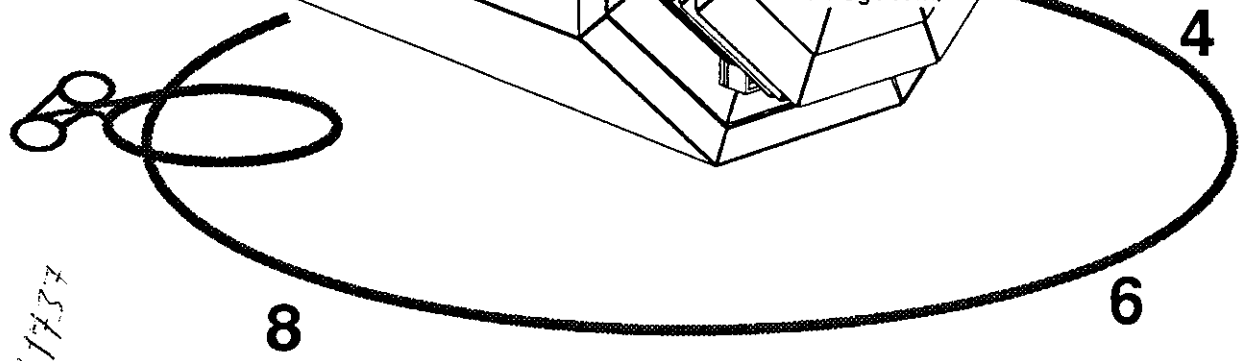
The L3P Collaboration

T. Aziz, R. Bock, W. Braunschweig, E. Geulig, K. Hilgers, H. Hillemanns, W. Karpinski, O. Kornadt, W. Krenz, Th. Lehmann, B. Lindemann, K. Lübelsmeyer, A. Nippe, D. Pandoulas, Y.J. Pei, M. Röhner, D. Schmitz, M. Schoentag, A. Schultz v. Dratzig, J. Schwenke, G. Schwering, R. Siedling, K. Subhani, M. Toporowsky, W. Wallraff, A. Weber, N. Xiao, Y. Zeng, J.F. Zhou, S. Zitzen
I. Physikalisches Institut, RWTH, W-5100 Aachen, FRG

J.J. Blaising, G. Coignet, A. Degré, M. Lebeau, D. Perret-Gallix, M. Schneegans
Laboratoire de Physique des Particules, LAPP, F-74941 Annecy-le-Vieux, France

C.Y. Chien, P.H. Fisher, T. Paul, A. Pevsner, C. Spartiotis
Johns Hopkins University, Baltimore, MD 21218, USA

G. Polivka, R. Rickenbach, M. Steinacher, L. Tauscher
University of Basel, CH-4056 Basel, Switzerland

J.Z. Bai, C. Chen, G.M. Chen, H.S. Chen, S.N. Chen, G.L. Dai, C. Fang, J.T. He, X.Q. Hu, B.N. Jin, H.B. Lan, B.M. Li, H.T. Li, R.B. Li, H.M. Liu, Y.S. Lu, J.M. Ma, Y.F. Mao, Y.H. Qu, J. Shen, X.W. Tang, K.L. Tung, F. Wang, J.H. Wang, C.L. Wei, R.J. Wu, P.P. Xie, J. Yan, C.G. Yang, K.S. Yang, Z.Q. Yu, G.R. Zheng, G.Y. Zhu, B. Zhang
Institute of High Energy Physics, IHEP, Beijing, China

F. Block, D. Boscherini, G. Bruni, P. Bruni, G. Cara Romeo, M. Chiarini, F. Cindolo, F. Ciralli, S. D'Auria, C. Del Papa, F. Frasconi, P. Giusti, G. Iacobucci, G. Levi, G. Maccarone, A. Margotti, T. Massam, R. Nania, F. Palmonari, G. Sartorelli, R. Timellini, S. Tzamarias
INFN Sezione di Bologna and University of Bologna, I-40126 Bologna, Italy

T. Aziz, S. Banerjee, S.R. Chendvankar, P.V. Deshpande, S. Dutta, S.N. Ganguli, S.K. Gupta, A. Gurtu, M. Maity, S. Mangla, K. Mazumdar, R. Raghavan, S. Sarkar, K. Sudhakar, S.C. Tonwar
Tata Institute of Fundamental Research, Bombay 400 005, India

S. Ahlen, A. Marin, B. Zhou
Boston University, Boston, MA 02215, USA

C. Coca, T. Angelescu, E. Halasz, N. Gheordanescu, A. Mihul, D. Pop
Institute of Atomic Physics and University of Bucharest, Bucharest, Romania

T. Csörgő, I. Horvath, P. Lévai, M. Prisznyák, J. Tóth, J. Zimányi
KFKI Research Institute for Particle and Nuclear Physics, H-1525 Budapest 114, Hungary

A.L. Anderson, U. Becker, P. Berges, J.D. Burger, M. Capell, Y.H. Chang, J. Chen, M. Chen, S. Chung, I. Clare, R. Clare, T.S. Dai, F.J. Eppling, A. Klimentov, V. Koutsenko, T. Kramer, A. Kunin, A. Lebedev, D. Luckey, A. Rubbia, M.S. Sarakinos, S. Shotkin, B. Smith, M. Steuer, S.C.C. Ting, S.M. Ting, Y.F. Wang, B. Wyslouch
Massachusetts Institute of Technology, Cambridge, MA 02139, USA

V. Gantmaher, V. Grazjilis, N. Klassen, Yu. Ossipyan, I. Schegelev, V. Timofeev
Institute of Solid State Physics, Chernogolovka, Russia

T. Barillari, M. Schioppa, G. Susinno
INFN Gruppo Collegato di Cosenza and Università della Calabria, Cosenza, Italy

O. Adriani, M. Bocciolini, A.M. Cartacci, G. Ciancaglini, C. Civinini, R. D'Alessandro, G. Landi, M. Lenti, M. Meschini, G. Passaleva, M. Pieri, V. Pojidaev, P. Spillantini
INFN Sezione di Firenze and University of Florence, I-50125 Florence, Italy

G. Anzivino, S. De Pasquale, L. Votano
INFN Laboratori Nazionali di Frascati, Frascati, Italy

J. Alcaraz, G. Brugnola, N. Colino, M. Felcini, V. Innocente, M. Marino, M. Pieri, J. Salicio, A. Zichichi
European Laboratory for Particle Physics, CERN, CH-1211 Geneva 23, Switzerland
The CERN group acknowledges the important contributions made to this Letter of Intent by:
F. Anselmo*, R. Barillère, A. Contin*, R. De Salvo*, H. Gerwig, P. Ford*, A. Hervé, G. La Commare*,
H. Larsen*, G. Laurenti*, P. Lecoq, J.M. Le Goff, C. Nemoz*, C. Williams*, F. Wittgenstein (* CERN - LAA)

M. Bourquin, W.J. Burger, D. Duchesneau, P. Extermann, J. Field, G. Forconi, D. Goujon, H. Hoorani,
J. Perrier, G.F. Susinno, M. Zofka
University of Geneva, CH-1211 Geneva 4, Switzerland

R. Ayad, J.Z. Bai, B. Bencheikh, X.D. Cai, U.K. Chaturvedi, W.Y. Chen, X.T. Cui, X.Y. Cui, M.T. Dova,
C. Gu, A.H. Hasan, D. Hatzifotiadou, H.L. He, G. Hu, R.A. Khan, M. Kaur, S. Khokhar, J. Lamas Valverde,
E. Leon Florian, Q. Lin, L.B. Liu, Y. Mi, Y. Mir, N.E. Moulai, M.A. Niaz, S. Qian, K.N. Qureshi, Z. Ren,
H.A. Rizvi, R. Sehgal, Y.M. Shabelski, J.Y. Sun, L.Z. Sun, A.A. Syed, P. Vikas, U. Vikas, M. Wadhwa,
K.L. Wang, Z.M. Wang, S.X. Wu, X.M. Xia, C.Y. Yang, G. Yang, C.H. Ye, Q. Ye, Y. Ye, J.M. You,
N. Yunus, G.Y. Zamora, M. Zeng, Z.P. Zhang, M. Zhao
World Laboratory, Lausanne, Switzerland

Q. An, H.F. Chen, Q. Gao, Z.F. Gong, C.H. Gu, Y. Jiang, C. Li, Z.Y. Lin, Y.Y. Liu, W.Z. Lu, W.G. Ma,
L.Z. Sun, C.R. Wang, Y.F. Wang, Z.M. Wang, J. Wu, Z.Z. Xu, B.Z. Yang, J.B. Ye, S.W. Ye, Z.P. Zhang,
M.H. Zhou
Chinese University of Science and Technology, USTC, Hefei, Anhui 230 029, China

J. Sarvas
Rolf Nevanlinna Institute, Helsinki, Finland

J. Heikkonen, P. Koikkalainen, H. Kälviäinen, J. Lampinen, E.Oja
Lappeenranta University of Technology, Lappeenranta, Finland

Ph. Rosselet
University of Lausanne, CH-1015 Lausanne, Switzerland

H. El Mamouni, P. Lebrun, J.P. Martin
Institut de Physique Nucléaire de Lyon, IN2P3-CNRS/Université Claude Bernard, F-69622 Villeurbanne, Cedex, France

M. Aguilar-Benitez, P. Arce, J. Berdugo, C. Burgos, M. Cerrada, B. de la Cruz, D. Fernandez, G. Fernandez,
P. Garcia-Abia, E. Gonzalez, P. Ladron de Guevara, C. Maña, F.J. Rodriguez, L. Romero, J.M. Salicio,
C. Willmott
Centro de Investigaciones Energeticas, Medioambientales y Tecnologicas, CIEMAT, E-28040 Madrid, Spain

A. Baschirotto, M. Bosetti, R. Castello, S. Pensotti, P.G. Rancoita, M.Rattaggi, G. Terzi
INFN Sezione di Milano and University of Milan, I-20133 Milan, Italy

D.Yu. Akimov, A. Arefiev, A.I. Bolozdynya, D.L. Churakov, Yu. Galaktionov, A. Klimentov, Yu. Kolotaev,
V. Koutsenko, A. Kunin, A. Malinin, V. Plyaskin, V. Pojidaev, A. Rozjkov, E. Shumilov, V. Shoutko,
I. Vetlitsky, I. Vorobiev
Institute of Theoretical and Experimental Physics, ITEP, Moscow, Russia

L.A. Bragin, N. Chernoplekov, I. Karpushov, E. Klimenko, S. Lelekhov, A. Malofeev, V. Mokhnatuk,
S. Novikov, E. Velikhov
Russia Scientific Center "Kourchatov Institute", Moscow, Russia

A. Aloisio, M.G. Alviggi, E. Brambilla, G. Carlino, R. de Asmundis, S. Lanzano, L. Lista, P. Paolucci,
S. Patricelli, D. Piccolo, C. Sciacca
INFN Sezione di Napoli and University of Naples, I-80125 Naples, Italy

P. Razis
Department of Natural Sciences, University of Cyprus, Nicosia, Cyprus

J. Seguinot, T. Ypsilantis
Collége de France, Paris, France

G. Gratta, M. Gruenewald, D. Kirkby, R. Mount, X.R. Shi, C. Tully, C. Zaccardelli, R.Y. Zhu
California Institute of Technology, Pasadena, CA 91125, USA

R. Battiston, G.M. Bilei, M. Caria, B. Checcuci, S. Easo, V. Krastev, M. Pauluzzi, L. Servoli, S. Wang
INFN Sezione di Perugia and Università Degli Studi di Perugia, I-06100 Perugia, Italy

L. Cifarelli
University of Pisa, Pisa, Italy

I.C. Brock, A. Engler, T. Ferguson, R.W. Kraemer, M. Merk, G. Tsipolitis, H. Vogel
Carnegie Mellon University, Pittsburgh, PA 15213, USA

P. Denes, V. Gupta, P.A. Piroué, H. Stone, D.P. Stickland, D. Wright
Princeton University, Princeton, NJ 08544, USA

J. John, P. Kozma, D. Richter, F. Spurný, V. Streit, M. Vomacka
NPI, 25068 Rez near Prague, Czechoslovakia

L. Barone, B. Borgia, F. Cesaroni, F. DeNotaristefani, M. Diemoz, C. Dionisi, S. Falciano, E. Leonardi,
E. Longo, C. Luci, L. Luminari, G. Mirabelli, G. Organtini, M. Rescigno, E. Valente
INFN Sezione di Roma and University of Rome, "La Sapienza", I-00185 Rome, Italy

V. Andreev, G. Alkahazov, A. Bykov, P. Kapinos, V. Kim, A. Tsaregorodtsev, A. Vorobiev, Yu. Zalite
Nuclear Physics Institute, St. Petersburg, Russia

X.L. Fang, C.D. Feng, X.Q. Feng, H.X. Gao, M. Gao, P.X. Gu, J.K. Guo, C.Q. Hu, Y.L. Hu, S.K. Hua, P.J. Li,
Z.D. Qi, D.Z. Shen, E.W. Shi, W.T. Su, X.X. Wang, Z.Y. Wei, Y.Y. Xie, L. Xu, Z.L. Xue, D.S. Yan, Z.W. Yin,
X.L. Yuan, Y.F. Zhang, G.M. Zhao, Y.L. Zhao, W.Z. Zhong, R.M. Zhou
H.C. Chen, W.Z. Chen, Z.M. Chen, Z.S. Ding, M.Z. Ge, Z.Y. Guo, G.Y. Han, J.R. Han, M. He, M.H. Jiang,
M. Jin, H. Li, Q. Li, Y.N. Liang, G.L. Liu, D.H. Nan, H. Pan, C. Qian, J.S. Qu, H. Shen, Y. Tang, C. Si,
C.R. Wang, R. Wang, W.M. Wang, W.M. Wu, S. Xie, B. Xu, W. Yang, Q. Ye, C.Y. Yin, B.T. Yu, C.W. Yu,
C.Z. Zhang, N.J. Zhang, S. Zhang, X.S. Zhang, X.Y. Zhang, S.M. Zhou
Shanghai Institute of Ceramics and Chinese Collaboration on Scintillating Materials, China

A.H. Walenta
University of Siegen, Siegen, FRG

N. Shivarov
Bulgarian Academy of Sciences, Institute of Mechatronics, BU-1113 Sofia, Bulgaria

M.T. Choi, J.K. Kim, Y.G. Kim, S.C. Kim, D. Son
Center for High Energy Physics, Taejon, Korea

A. Chen, L.S. Hsu, Y.Y. Lee, W.L. Lin, W.T. Lin, W.T. Ni, S. Su, Y.C. Yang, S.C. Yeh, H.C. Yen
High Energy Physics Group, Taiwan, China

A. Koski, L. Kettunen, R. Mikkonen, N. Ojala
Tampere University of Technology, Tampere, Finland

D. DiBitonto, T. Pennington, K. Subhani, Y. Takahashi
University System of Alabama, Tuscaloosa, AL 35486, USA

A. Bujak, D.D. Carmony, L.J. Gutay, T. McMahon, B.C. Stringfellow
Purdue University, West Lafayette, IN 47907, USA

H. Anderhub, F. Behner, J. Behrens, B. Betev, A. Biland, M. Dhina, R. Eichler, G. Faber, K. Freudenreich,
C. Grab, M. Hänsli, H. Hofer, I. Horvath, M. Jongmanns, P. Lecomte, P. LeCoultre, M. MacDermott,
M. Maolinbay, P. Marchesini, D. McNally, F. Nessi-Tedaldi, C. Neyer, J. Paradiso, F. Pauss, M. Pohl,
G. Rahal-Callot, D. Ren, J. Riedlberger, N. Scholz, U. Röser, H. Rykaczewski, H. Suter, J. Ulbricht,
G. Viertel, H.P. Von Gunten, S. Waldmeier, J. Weber, P. Zemp
Eidgenössische Technische Hochschule, ETH Zürich, CH-8093 Zürich, Switzerland

Contents

CHAPTER I
Physics at LHC with the L3P Detector
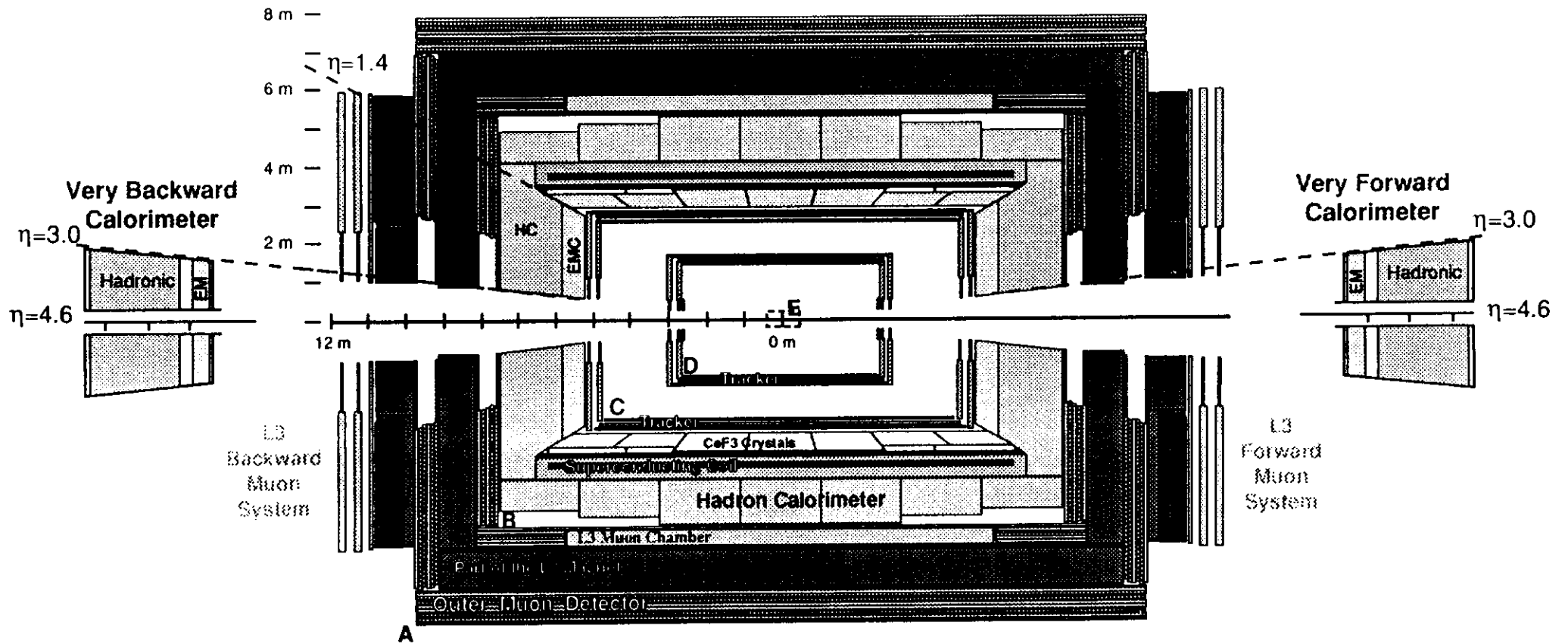
Figure 1. Cross-sectional view of the Detector
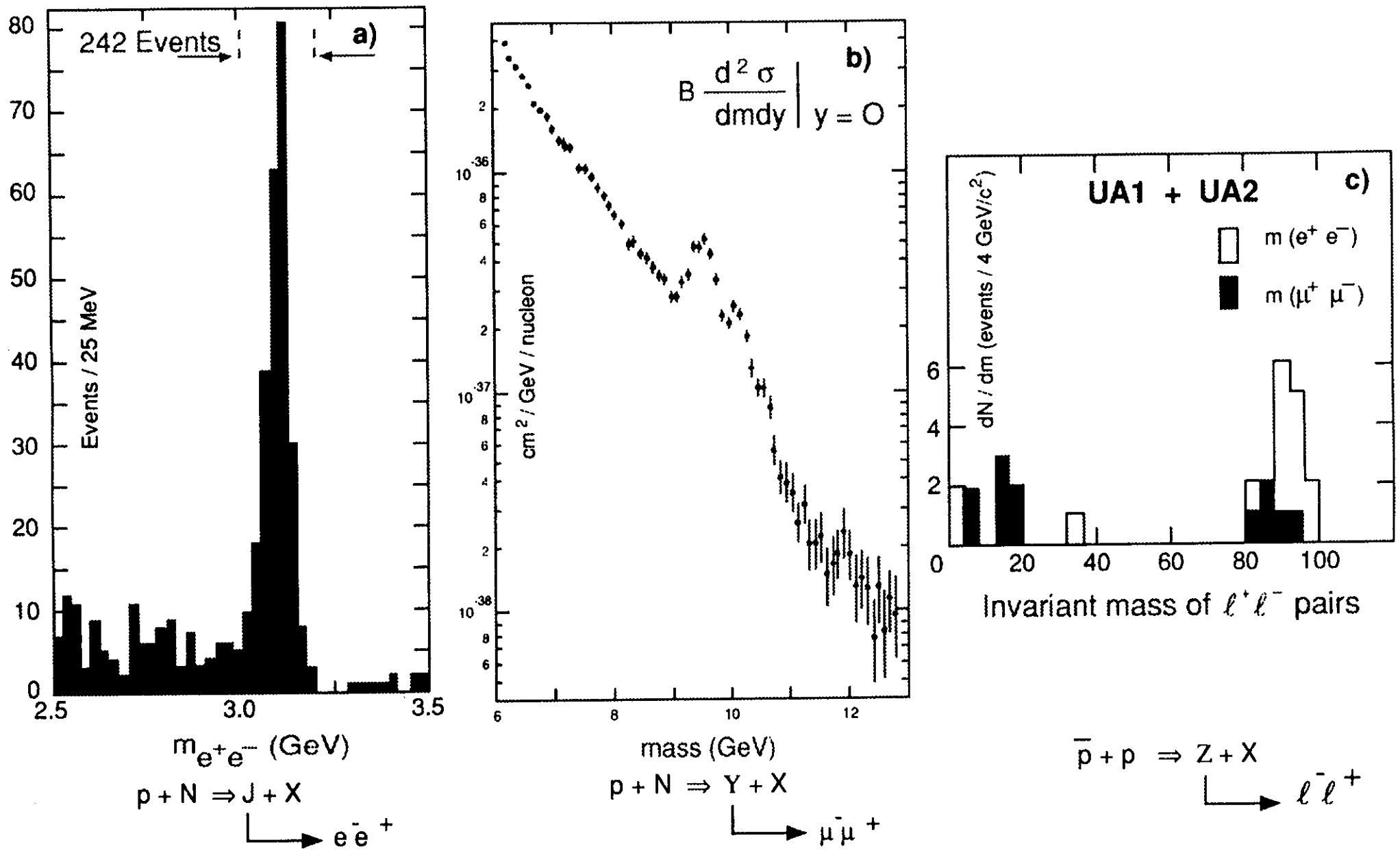
Figure 2 :

Some Physics Results from Measuring Electrons and Muons

1. PHYSICS AT LHC WITH THE L3P DETECTOR

1.1. Physics Objectives

The great efforts made at CERN on the construction of a Large Hadron Collider (LHC) at a center mass energy of 16 TeV and ultimate luminosity of $4 \times 10^{34} cm^{-2} s^{-1}$ will enable physicists to explore competitively new frontiers of physics.

The plan to use the existing LEP tunnel and much of the existing CERN-LEP infrastructure implies that LHC will be constructed in an economical and timely way.

In this LOI, we propose to construct a general purpose detector (see Fig. 1), which will have a unique high resolution in measuring electrons, photons and muons, using much of the existing L3 equipment and infrastructure. **The physics objectives of L3P are not only to search for particles predicted by current theories, such as the Higgs boson, but more important, to look for unexpected phenomena.** The spirit of this effort is to propose a detector which is complementary to other detectors at the SSC, Tevatron and LHC. The design is based on a realistic assessment of the very high LHC background situation and on our efforts in studying e, μ, γ, including the L3 experiment and the successful design of L^* at the SSC. It is our intention to ensure that a powerful detector will be available for physics at LHC turn on.

1.2. Physics Considerations

Over a period of a quarter of a century, there have been many fundamentally important discoveries in elementary particle physics. These discoveries, which gave us confidence in the Standard Model, were all made by precision experiments on leptonic and photonic final states. Indeed, one can recall the following examples :

1. The discovery of two kinds of neutrinos [1] came from measuring μ and e final states.

2. The discovery of the J particle [2] shown in Fig. 2a was done by an experiment on e^+e^- final states with a mass resolution of 0.1 % and a hadron background rejection of $1/10^{10}$.

3. The τ lepton [3] was discovered with a detector measuring the coincidence of μ,e final states.

4. The discovery of the P_c state by the DASP Collaboration [4] at DORIS in July 1975 from a very clear and elegant observation of the 2γ transition of the ψ' is one of the most important confirmations of the existence of charm quarks.

5. The Υ particle [5] (Fig. 2b) was discovered by an experiment with a μ pair mass resolution of 2 %.

6. The proof that the J particle is indeed a bound state of $c\bar{c}$ quarks comes from precision inclusive photon measurements with NaI crystals by the Crystal Ball group [6]. The identification that the Υ particle is from a bound state of $b\bar{b}$ quarks comes from inclusive photon measurements by the CUSB [7] and CLEO groups [8] as well as by the ARGUS and Crystal Ball groups [9].

7. The pioneering study of e^+e^- pairs at the ISR by the CCR and CCOR groups contributed fundamentally to the understanding of the production mechanism of new particles (J, Υ) at high energies [10].

8. The discovery of the Z^0 particle [11] (shown in Fig. 2c) was done with large solid angle detectors measuring e^+e^- and $\mu^+\mu^-$ final states.

9. The $W^\pm$ [12] was found by measuring its large momentum single electron and muon decays.

These facts lead us to make the following observations :

- These discoveries were not predicted when the original accelerators were constructed (the Z and W excepted).

- None of these discoveries were made by detecting hadronic final states.

- In general, the decay rate of heavy particles into single lepton, single photon and lepton pairs is much smaller than the decay rate into hadrons. However, since the background from large momentum transfer single leptons or single photons and high mass lepton pairs is generally very small, if an experiment can be done cleanly and precisely, with good resolution and good hadron rejection, one can

1

clearly distinguish the signals from the background, as shown in Figs. 2a to 2c.

1.3. Design Considerations

In high luminosity hadron colliders such as the ISR as well as stationary target experiments with high intensity beams, $10^{10} - 10^{12}$ppp on target (with equivalent luminosity of 10^{34} and higher), the background was always much higher than anticipated. Monte Carlo calculations of background can only be used as a lower order estimation of the background. Part of the reason is because the yields of photons, electron pairs and muon pairs are many orders of magnitude lower than the yields of hadrons. In addition, there are always abundant amounts of muons, photons and neutrons traveling along the beam and entering into the detectors. It is often very difficult to trace the origin of these particles.

The following experiments serve as examples for designing a precision lepton and photon pair experiment at LHC :

1. **Test of Quantum Electrodynamics and study of leptonic decays of vector mesons at DESY.** A series of experiments [13] were done in a high intensity beam of 10^{11} photons per second. The detector had a mass resolution of $\Delta M/M \approx 1$ % and a hadron rejection of $ee/hh = 1/10^8$. The key elements of these experiments were such that :

   (a) The detectors were far away from the target and no material was placed between the target and the detector to prevent π° conversion.

   (b) Strong magnetic field between the target and the first detector elements swept away low energy particles.

   (c) Electrons were measured twice : first the momentum (p) was measured by magnetic spectrometers with threshold Cerenkov counters and second the energy (E) was measured by shower counters. The requirement p = E eliminated most of the backgrounds.

   (d) The minimum transverse distance between the detector and the beam line was ≈ 2 meters therefore the beam spray did not enter into the detector.

2. **Discovery of the J particle at Brookhaven.** This experiment [2] was carried out in a high intensity proton beam of 10^{12} protons per second, equivalent to a luminosity of $10^{36}cm^{-2}s^{-1}$.

   The key elements of this experiment were :

   (a) Strict application of the experience learned at DESY (see above) by locating the detector far away from the target to eliminate the beam spray (the minimum distance between the detector and the beam line being again ≈ 2 meters) and by minimizing the material in front of the detector to reduce the π° conversion and knock-on electrons. Indeed, it was the development at CERN of hydrogen gas Cerenkov counters, with 3mm spherical collecting mirrors and $125\mu m$ mylar windows at each end of the counters, that made this experiment possible.

   (b) Development of high rate proportional chambers to operate at low voltage and orientate the wires 120° apart with the result that these chambers (size 1 m^2) could work at 20 MHz and were able to reconstruct the trajectory without ambiguity.

3. **Discovery of the Υ particle at Fermi National Laboratory.** This experiment [5] had a mass resolution of 2 % using $(1.5-3) \times 10^{11}$ incident protons per accelerator cycle. The proton intensity was limited by the requirement that the single rates at any detector plane not to exceed 10^7 counts per second.

   The mass resolution of 2 % was obtained by measuring muon trajectories in free space. The identification of muons was done by measuring muons with an accuracy of ≈ 15 % (at 10 GeV) using trajectory information in a magnetized iron absorber. The minimum distance between the first counter and the beam line was again ≈ 1 meter.

4. **Muon pair study at the ISR.** This was a 2π detector [14] measuring muon pair production with a luminosity of $\approx 10^{32}$. This experiment was carried out with the classical method of measuring muons with magnetized iron sandwiched with large drift cham-

bers. Whereas the result of this experiment provided very accurate information in studying $pp \rightarrow \mu\mu + X$ scaling precisely, it also revealed the great difficulty of aligning large area drift chambers sandwiched in a closed area between magnetized iron. We learned that, in practice, it was difficult to align large area chambers $(3 \times 6m^2)$ to better than $\approx$ 1mm, with the result that the momentum resolution was considerably worse than that of the original design value.

5. **The L3 experiment at LEP.** Nearly all the physicists in this LOI participated in building a 4π detector (L3) [15] which measures a 100 GeV particle decaying into a pair of muons with a mass resolution of 1.7 %. L3 also measures electrons and photons with a coordinate resolution of $\approx$ 1mm, an energy resolution of 5 % at 100 MeV and an energy resolution of 1.3 % at 2 GeV. The L3 detector has a good hadron rejection. The momentum of $\mu(e)$ is measured twice, first in the vertex chamber with a value of P, and second, by the precision muon chambers with a value P_μ, or in the BGO with a value P_e. The muon energy loss ΔE is measured by the sampling calorimeter which also monitors hard photon radiation. The energy balance, $P = \Delta E + P_\mu$ or $P = P_e$ eliminates the backgrounds efficiently.

From the above five examples, we conclude that a high precision detector to measure e, μ, γ at LHC should have the following characteristics :

1. **To reduce the beam spray** : the transverse distance for most of the detector elements should be as far from the beam line as possible.

2. **To reduce neutral particle background** : all elements should be far away from the intersection point.

3. **To reduce charged particle backgrounds** : a strong magnetic field surrounding the intersection region is necessary.

4. **To reduce background on photons** : the individual electromagnetic calorimeter elements should be far away so as to separate the 2 γ rates from π^0 decay and there should be a minimum of material before the electromagnetic detector.

5. **To reduce background on electrons** : the momentum of the electron (p) defined by electron trajectories in a magnetic field and the energy of the electron (E) defined by pulse height with the individual electromagnetic calorimeter elements should be both measured with high accuracy, so that p = E can be satisfied to the 1 % level.

6. **To reduce background on muons** : the momentum of muons should be measured repeatedly $(\vec{p_1}, \vec{p_2}...\vec{p_n})$. The most precise momentum measurement $(\vec{p_1})$ can only be done by measuring trajectories in free space. Other measurements $\vec{p_2}$ to $\vec{p_n}$ to $\approx$ 10 % level are used to reject background by the constraint : $\vec{p_1} = \vec{p_2} = \vec{p_n}$.

1.4. Technical Considerations

A realistic design of a large experiment must also take into consideration the ability to build the detector on time. Therefore, one must take into account the following :

1. **Technical Capability** : Many physicists in this collaboration have continued R&D efforts on precision instrumentation in muon physics, in new crystals and in mass production of high quality crystals for electron and photon physics and in calorimetry. In the following we give some examples (limited by space considerations),

   (a) **precision instrumentation on muon physics** : over a period of 20 years, we have continued intensive R&D efforts [16] to develop precision instrumentation for muon physics. This includes the following :

      • Alignment systems : development of high precision alignment systems ($5\mu m$ precision) with UV laser verification.

      • Chamber construction : development of methods to build high resolution muon chambers covering an area of $\approx$ 1,000m^2 with $30\mu m$ precision.

      • Supporting structures : development of supporting structures for precise alignment of the chambers ($10\mu m$ reproducibility).

3

- Gas study : selection of the gases for large area drift chambers in a magnetic field, and particularly non-flammable gases.

The success of this program is the main reason why we were able to build the precision muon system in L3, and our continued effort on muon R&D gives us confidence to be able to construct a precision muon system for L3P.

(b) **precision instrumentation on electron and photon physics** : Since most of the rare earth materials are produced in China and there are many excellent centers for crystal studies there (Shanghai Institute of Ceramics, Shandong University, Zhejiang University and Beijing Glass Institute) as well as an excellent research center in Russia (Institute of Solid State Physics, Moscow), we have continued large scale systematic efforts in developing new crystals and on mass production at low cost of radiation resistant crystals. The Chinese effort, under the coordination of Professor D.S. Yan, and the Russian effort coordinated by Academician Yuri Ossypian, have been most successful. We are now confident to be able to produce large amounts of crystals for the L3P experiment.

(c) **silicon calorimetry** : A large systematic effort on the properties of silicon calorimetry, VLSI readout associated electronics and radiation effects on both detectors and electronics has been carried out by the SICAPO group [17]. Currently an intensive R&D program lead mainly by the INFN (Florence, Milan and Rome) groups in L3 and by the Dubna group is achieving the required low cost for mass production on both silicon detectors and associated VLSI readout electronics, as well as on silicon detector plane assembly.

2. **Engineering Resources** : The construction of large experiments depends on a good collaboration between engineers and physicists. Over the last 10 years, the L3 collaboration has assembled a large group of engineers and technicians from leading physics institutions all over the world (member states of CERN, Russia, China and the U.S.). It has taken many years to establish mutual understanding and collaboration among these engineers and technicians who are now familiar with each others measurement systems and practices. The ability of this group of engineers and technicians must be taken into consideration in determining the complexity of the final detector.

1.5. Financial Considerations

Our experience in the construction of L3 and in designing $L^\star$ enables us to realize that much effort must be spent in understanding and controlling the cost of general purpose detectors at LHC. The enormous costs of the SSC and LHC detectors will ultimately determine their completion date. With limited financial resources available, it is important for us to design a detector, taking into account the following :

1. **Use as much as possible of the existing L3 equipment and infrastructure.**

2. **Construct the detector in phases** but ensuring that a powerful detector will be available at LHC turn-on.

1.6. The L3P Detector

Based on the above considerations, we present the design of the L3P detector in Fig. 1. It has the following unique features :

1. The central trackers (C) and (D) are far away from the colliding proton beams. Most parts of the first detector (D) (made out of proportional chambers, drift tubes and gas microstrip detectors) are located at least 1.65 meters away from the proton beam (see Chapter 3). Even the very forward region near $|\eta| = 3$ made out of the gas microstrip detectors is located 50 cm away from the beam.

The entire tracker (260 m^3) can be removed and a new tracker can be installed for specialized physics research, such as heavy ion physics. Indeed, the volume is large enough to accomodate most of the dedicated heavy ion detectors presented in the LHC EOI meeting in Evian, France.

4

2. We shall use crystals from China (for example CeF_3), specially made for L3P, for the region $|\eta| \leq 1.4$. In the forward-backward region $1.4 \leq |\eta| \leq 3.0$, a sampling calorimeter will be used (see Chapter 4).

3. The total amount of material in front of the crystals and the electromagnetic sampling calorimeter is less than 3 % X_0.

4. Low energy charged particles will be swept away by a 2 - 3 T magnet with a 7 meter inner diameter and a 13 meter length. The 2 -3 T field magnet means that it can be constructed economically and reliably. The combination of large empty ($\approx 50m^3$) volume around the interaction point with a 2 - 3 T field implies very low rate in the trackers.

5. **Photons** are measured by the electromagnetic crystal calorimeter, located at a minimum ≈ 3 meters away from the intersection point. At this large distance, the knowledge of shower profiles from crystals yields accurate information on the photon production angle. This large distance also implies that a 25 GeV $\pi^\circ \rightarrow 2\gamma$ will produce two separate shower peaks and thus can be rejected. The large distance also implies that the neutral background on the crystal surface will be minimized (see Chapter 4).

6. **Electrons** are measured twice, first from momentum information in the trackers (C) and (D) to an accuracy of 1 % (100 GeV). This will be matched with energy information obtained from the pulse height measurement to an accuracy of ≈ 1 % at 100 GeV (see Chapter 4).

   In the second phase of L3P with the completion of the central tracker with a 3 T field, the electron momentum will be measured with an accuracy of 3.6/1000 (see Chapter 12).

7. **Hadrons** are measured by a sampling calorimeter (total absorption $\geq 9\lambda$) which is constructed similarly to the L3 detector, with read-out towers pointing to the intersection region (see Chapter 5). It provides complete η coverage up to $\eta = 4.6$ (see Chapter 7).

8. **Muons** are measured independently three times :

(a) with multi-layer drift tubes (A), existing L3 muon chambers (B), central tracker (C & D), together with vertex information (E) given by LHC (see Chapters 3 and 6).

Typically, if we use the 3 T (2 T) magnet for 100 GeV muons we have :

$$(\tfrac{\Delta p}{p})_1 \approx 0.7\%(1\%)$$

(b) Measurements (A, B, C and E) without inner tracker (D) yield :

$$(\tfrac{\Delta p}{p})_2 \approx 4\%(6\%)$$

(c) Measurements from stations A, B combined and E yield :

$$(\tfrac{\Delta p}{p})_3 \approx 10\%(14\%)$$

The requirement $\vec{p_1} = \vec{p_2} = \vec{p_3}$ eliminates most of the backgrounds.

In the second phase of L3P, with the completion of the central tracker with a 3 T field, the muon momentum will be measured to an accuracy of 3.6/1000 (see Chapter 12) and we shall have:

$$(\tfrac{\Delta p}{p})_1 \approx 0.36\%$$

$$(\tfrac{\Delta p}{p})_2 \approx 4\%$$

$$(\tfrac{\Delta p}{p})_3 \approx 10\%$$

9. Because the first detector element is far away from the beam, with the 3 T magnet the detector will be able to use the ultimate luminosity of $4 \times 10^{34} cm^{-2} s^{-1}$ for e, μ and γ physics.

10. The detector is designed to use much of the existing L3 infrastructure, the forward-backward muon chambers, a large part of the central muon chambers as well as the existing L3 magnet frame and toroidal doors.

To summarize, despite current financial limitations, the L3P Collaboration intends to construct, based on their past experience, a complementary detector to all other detectors, at the SSC, Tevatron and LHC. We intend to fully explore the potentials of LHC without compromises.
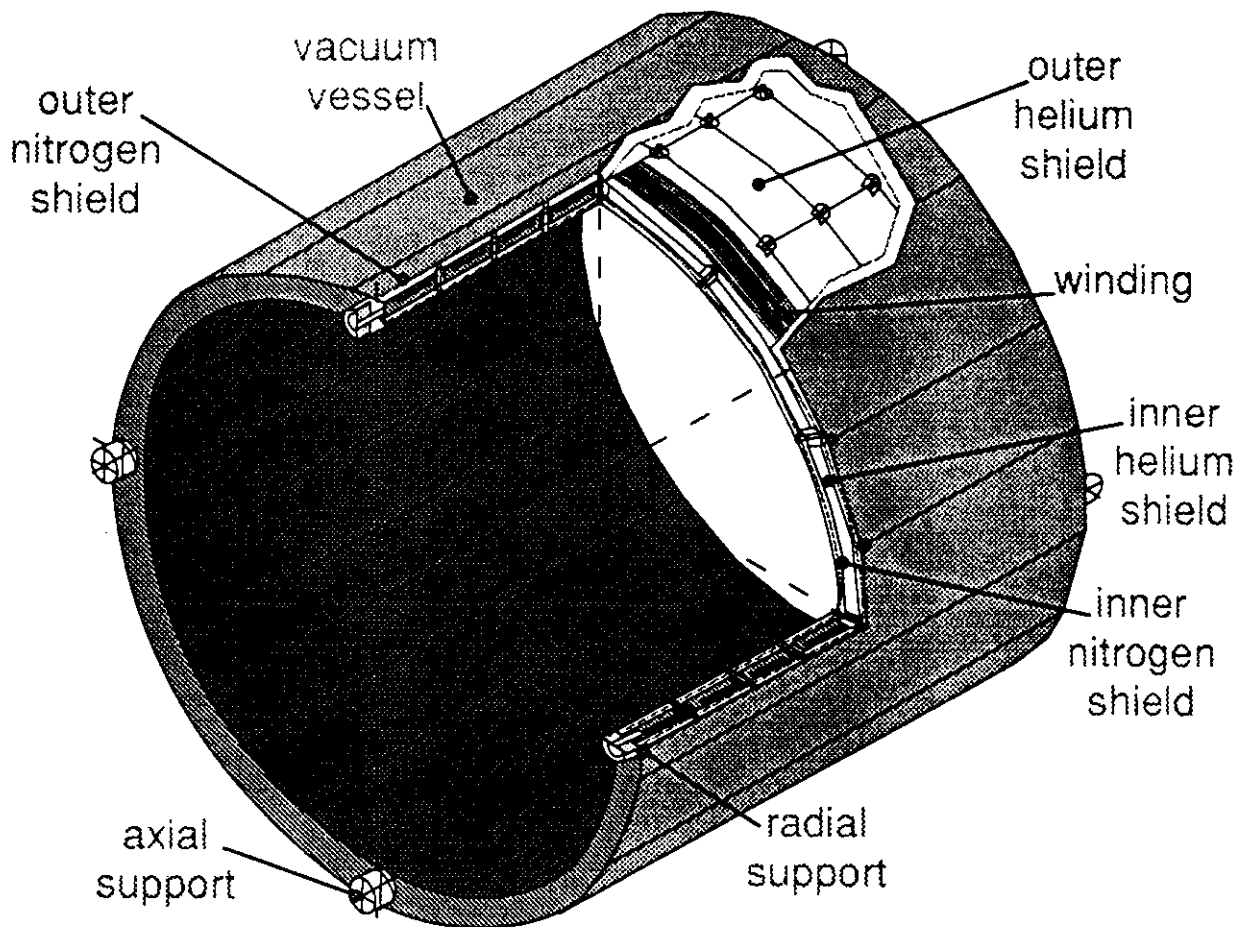
CHAPTER II
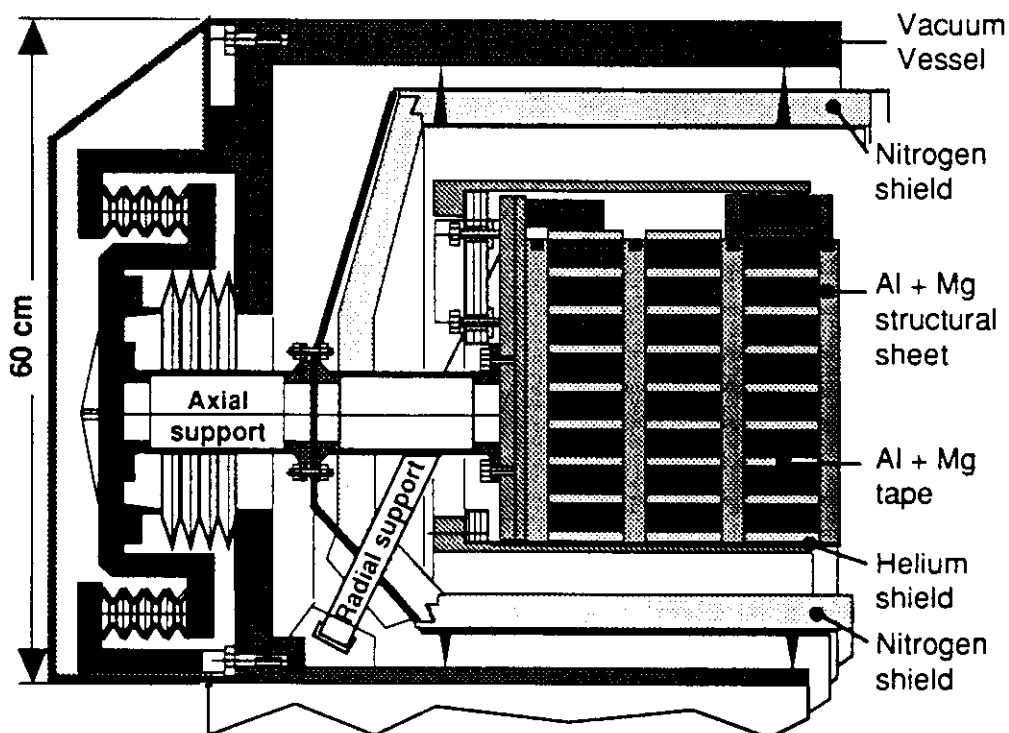## The Magnet System

Figure 3. The 2T Magnet Overview

Figure 4. The 3T Magnet cross section

2. THE MAGNET SYSTEM

2.1. General Magnet Design Considerations

The use of large superconducting magnets has increased in recent years, both in high energy physics and in fusion research. For example, ALEPH and DELPHI magnets are operating successfully at LEP/CERN, while the T-15 magnet [18] at the Kurtchatov Institute, the LCT coils [19] at ORNL and TORE SUPRA at Saclay are examples of magnets for fusion research.

In this LOI we consider two versions for the superconducting coil, a 2 T option (Fig. 3) and a 3 T (Fig. 4)), both having an inner free bore diameter of 7 m. The main advantage of the 2 T option is that the magnetic flux can be contained by the existing L3 iron barrel. Although the 3 T option requires additional iron in the barrel, it has the advantage of reducing the charged particle background significantly. Fig. 5 shows the background rate per crossing in the innermost tracking elements as a function of B. When increasing the field from 2 to 3 T the rate in the end-cap detector barely grows while the rate in the innermost barrel tracker element is reduced by 2.2. Beyond 3 T the background reduction becomes less important. The cost of the 3 T option is higher due to the additional cost of superconductor and structural material, and the iron to contain the increased return flux.

As seen from Fig. 5 the detector will be able to function at a maximum luminosity of $4 \times 10^{34} cm^{-2} s^{-1}$.

To minimize the thickness of the magnet we use pure Al as stabilizing material and Al-Mg alloy (thermally compatible with Al) as the structural material. The magnet thickness is $0.5 - 0.7 \lambda_{abs}$.

For this project we have followed a conservative approach by keeping the conductor in the elastic state to suppress mechanical perturbations and thus the admissible strain level has been limited to 0.1% which corresponds to a stress level of 60-70 MPa. To ensure a reliable operation one must:

- minimize possible thermal perturbations,

- ensure a high mechanical stability of the winding to prevent important mechanical perturbations,

- provide a stability margin for the conductor as high as compatible with a reasonable winding thickness.

Following the broad experience of the Kurchatov
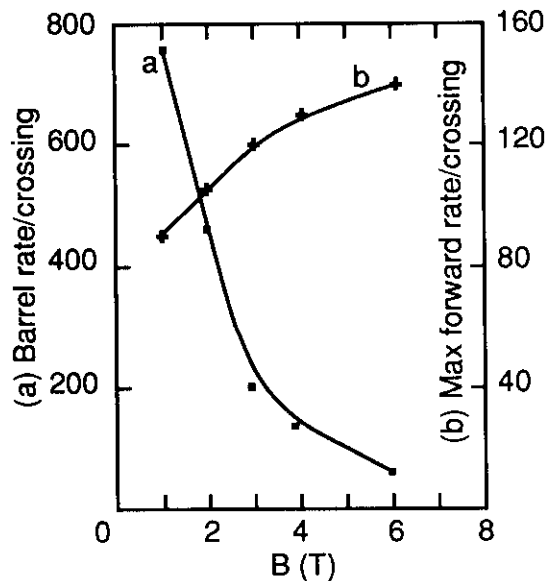
Figure 5: Background rate as a function of magnetic field B for a luminosity of $1 \times 10^{34} cm^{-2} s^{-1}$.

Institute in special adhesives for low temperature applications in superconducting coils, we will use adhesive foils developed by the aircraft industry. These foils provide thin adhesive layers, not prone to cracking, having a strength several times higher than the typical shear stress met in SC coils.

A common feature for both options is the use of recently developed Al stabilized conductors having a thin copper layer lined over the Al surface. This copper layer offers a good and reliable contact with the main metal ensuring high thermal diffusion, provides the possibility of soft soldering the conductor elements for manufacture, and simplifies the realization of low resistive current joints inside a winding. Table 1 shows the main parameters of the two options.

2.2. 2 Tesla Monolayer Solenoid
2.2.1. Magnet General Description

The layout of the solenoid is shown in Fig. 3 and its cross section in Fig. 6, while the winding characteristics are listed in Table 2.

The design is quite similar to the successfully operated ALEPH magnet. The monolayer winding of pure Al stabilized conductor is adhesively bonded to an Al-Mg support cylinder which takes a part of the radial magnetic pressure and almost

6

Table 1: Main parameters of the two magnet options.

Option	L3P 2 T	L3P 3 T
Vacuum vessel		
inner bore (m)	7.0	7.0
outer dia. (m)	8.0	8.2
length (m)	13.0	13.0
mass (t)	45	70
Cold mass (t)	100	220
Central induction (T)	2	3
Operating current (kA)	29	21
Stored Energy (GJ)	0.9	1.9
Magnet radial		
thickness (cm)	50	60
in nuclear interaction		
length (λ_{abs})	0.5	0.7
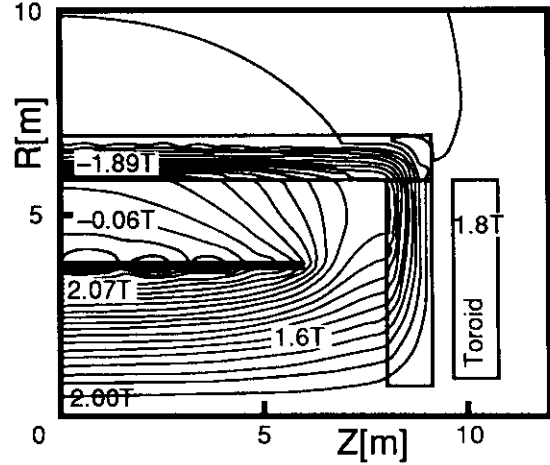
Figure 7: 2 T Magnetic Field Distribution.
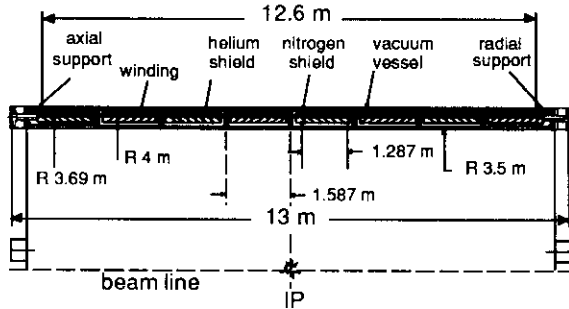
Figure 6: 2 T Magnet cross section.

Table 2: Winding characteristics of the 2 T option.

Type of winding	monolayer
Coil dimensions	
outer diameter of	
supporting cylinder (m)	7.60
winding outer dia. (m)	7.44
winding mean dia. (m)	7.38
length (m)	12.6
Sections	
number	8
winding length (m)	1.29
number of turns	100
length of conductor (km)	2.38
Inductance (H)	2.2
Dumping voltage (V)	± 600

the whole axial compressive force. This cylinder is cooled by the thermosiphon method and the conductor is indirectly cooled by thermal conduction through several layers of insulation. For a chosen operating current of $29kA$ the conductor current density can be as high as $40A/mm^2$ for $2T$ with a monolayer winding. Stability is ensured by providing a sufficiently high critical current margin, by protecting the conductor with LHe temperature shields, and by suppressing the mechanical perturbations by designing the conductor and the cylinder to a low stress level (Tresca equivalent stresses are limited to 60 and 104 MPa respectively). To ease manufacturing, transportation and assembly, the winding is subdivided into eight sections separated by 300 mm gaps, adjacent sections being fixed to each other by flanges. POISSON computations have shown a satisfactory magnetic field uniformity in the central tracker region as shown in Fig. 7.

The vacuum vessel is reinforced by seven spoke-like assemblies made from 50 mm bars (radial supports) connecting the inner and outer shells. Such a design allows the inner and outer shells to be as thin as 20 mm, while the average stress in the shells does not exceed 23 MPa.

The conductor parameters are listed in Table 3 and Fig. 8 shows the cross section. A Rutherford type cable, with strands of 1.3 mm diameter, is soldered between two copper clad pure Al profiles. The critical current for 3.1 T (which is the maximum field seen by a strand taking into account the

7

Table 3: Main parameters of the conductors.

Option	L3P 2 T	L3P 3 T
Dimensions		
thickness (mm)	12.2	20
width (mm)	60	40
SC wire	Nb-50% Ti	Nb-50% Ti
SC/Cu	2/3	2/3
diameter (mm)	1.29	1.29
number in cable	25	21
Critical current		
in max. field (kA)	55	42
Stabilizer	Cu clad Al	Cu clad Al
RRR	500	500
Overall conductor		
length(km)	19	37
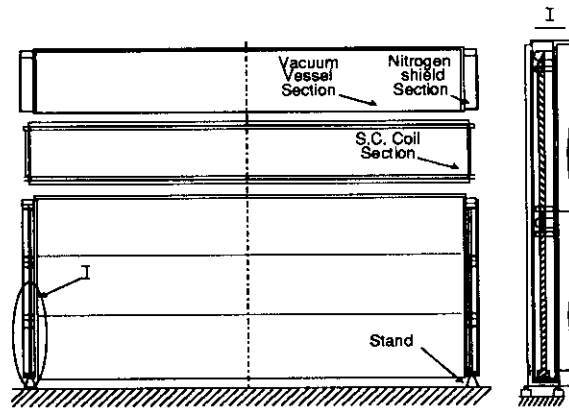
Figure 9: Assembly sequence of the 2 T magnet. On the righthand side a blowup of two coil sections is shown.
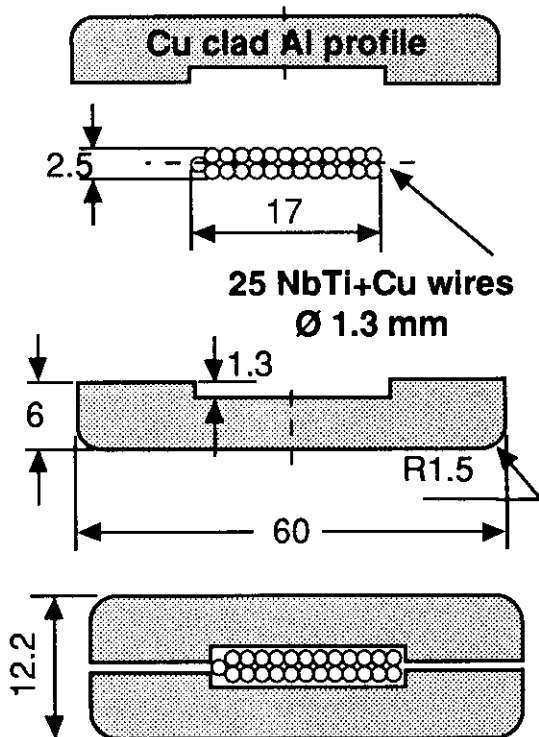
Figure 8: SC conductor.

self field) is twice the operating current. This provides a temperature margin of about 1 K, taking into account warming-up of the cylinder by eddy currents created when energizing the magnet in 2 hours, thus allowing a safe operation.

To ensure a high construction quality, the coil and the vacuum vessel sections, equipped with their radiation shield elements, will be manufactured at a company site. Possibilities do exist to air lift sections of such dimensions to CERN for the final assembly. The following vertical assembly procedure is proposed (Fig. 9):

- The end flange of the vacuum vessel with its radiation shield is installed onto a special support structure.

- The first coil section is installed onto the end flange by means of temporary supports and all permanent connections with the flange are fitted and tested.

- The first cylindrical section of the vacuum vessel is engaged onto the magnet section and is bolted to the flange.

- The second magnet section is installed on the first one, attached to it, and all cryogenic and electrical joints are welded or soldered and tested.

- The second cylindrical section of the vacuum vessel is engaged onto the second coil unit and is bolted to the first vacuum vessel section.

8

- These cycles are repeated until the vacuum vessel second end flange is installed and fastened.

- The vacuum vessel is finally closed with 18 circular joints by welding, and vacuum tests of the vessel can be performed.

- Cryogenic and field tests can be performed in the surface hall before lowering the magnet down to the pit.

2.2.2. Cryogenic System

In normal operation, the cryogenic heat loads are about 500 W. A cryogenic system (1 kW refrigerator, LHe vessel for thermosiphon, cooling and pipe lines) can operate in various regimes:

1. Pre-cooling of the winding with cold He gas.

2. Cooling by natural convection of He vapor-liquid mixture in the tubes attached to the support cylinder.

3. Warming-up of the winding with warmer He gas when necessary.

The pre-cooling requires about one week with a He gas flow of 0.25 kg/s. This rate is determined by the admissible level for the mechanical stresses inside the magnet structure, and for this, the temperature difference in the coil should not exceed 30 K around room temperature and 50 K around LN temperature. To absorb the transient heat load caused by eddy currents in the cylinder when energizing, an additional amount of 1500 l of liquid helium is needed.

2.2.3. Power Supply and Energy Dumping System

The magnet is energized with a stabilized semiconductor power supply (15 V/450 kW) in two hours, this rate being limited by the acceptable level for the eddy current losses (400 W).

When discharging, the high current density in the conductor does not allow the extraction of all the energy from the winding. A combined method of dumping is used. After breaking off the current supply circuit the current in the coil decreases but, due to eddy currents warming-up the cylinder to a much higher temperature than the conductor critical temperature, the winding becomes normal (quench-back effect). The coil discharge takes about 60 s for a maximum voltage not exceeding

Table 4: Winding characteristics of the 3 T option.

Type of winding	Double pancake
Coil	
inner bore (m)	7.23
outer dia (m)	7.83
winding mean dia (m)	7.53
length (m)	12.3
Pancakes	
number	92
number of turn in	
a double pancake	17
thickness (mm)	82
length of conductor (km)	0.4
Inductance (H)	8.6
Dumping voltage (V)	±600

$\pm 600V$. About $350MJ$ of the stored energy dissipate in the two dumping resistors (0.02Ω each). The same amount of energy dissipates in the winding and the remaining 200 MJ fraction dissipates in the support cylinder. The maximum temperature does not exceed 100 K and the maximum temperature difference between the winding and the cylinder stays below 45 K, which is quite admissible from the point of view of the mechanical strength of the adhesive.

2.3. 3 T Solenoid

A design for the 3 T option, with a pancake type winding, is shown in Fig. 4, the main parameters being listed in Tables 1, 3 and 4. To get a coil with sufficient strength to prevent mechanical perturbations, relative movements between the turns are excluded by fixing each turn by adhesive bonding to a disc shaped plate. All the winding elements (Al conductor, Al-Mg tape and Al-Mg plates) work together against the radial pressure (3.6 MPa) due to the magnetic field, and the hoop stress is distributed uniformly over the winding cross section. The role of these elements differs in resisting the axial force (13 MN). The plates and tapes (which are slightly wider than the conductor) form a stiff lattice carrying the main part of the axial load. The conductor, sitting inside these lattice cells, supports a reduced axial stress because it is surrounded by a low Young's modulus insulation layer. The conductor design is quite similar to the one previously described, but here we have more freedom to choose the cross section of the conductor. For this case the current density in the conductor can be

as low as $25 A/mm^2$, and no problem is expected for the magnet protection. The 92 double pancakes are axially compressed with two (inner and outer) sets of clamps then bonded together by gluing. LHe tubes are attached to the clamps which are in effect also used as LHe shields protecting the conductor against thermal leaks. To compensate the small difference in the thermal contraction coefficients of the glued winding and of the metal clamps, springy elements are placed at the ends of the coil between the clamps and the winding. As in the 2 T option the conductor is indirectly cooled from tubes glued to each plate. The thermal conductivity of the Al-Mg plate with adhesive layers is sufficient to provide pre-cooling of the winding in a week. The cryogenic system is the same as for the previous option. However the level of eddy current losses is lower because the electrical resistance of the disc-plate assemblies is much higher than the one of the solid support cylinder. The assembly of the magnet follows a conventional procedure. The coil and the vacuum vessel are assembled separately and the coil is inserted inside the vessel and hung by fiberglass rods. Movements in the axial direction are blocked by special fiberglass supports. However, as in this case there are no intermediate radial supports between the two shells, their thickness must be at least 48 mm. This brings, all in all, a 600 mm radial thickness for the 3 T option.

Design studies are in progress to decrease this value down to 500 mm. However, it is already clear that a straightforward extrapolation of today's proven techniques is not sufficient, and innovative solutions must be found. They must be the subject of R&D programs and qualification tests before they can be implemented. For example the problem of what is the acceptable stress level in a pure Al stabilized conductor must be understood.

2.4. Magnetic Flux Return Frame

For a large magnet the construction and assembly of the yoke in the underground area is the longest operation. As the existing iron yoke of L3 is used for L3P, with only a slight increase of the barrel thickness, this brings a decisive planning advantage. The cost of the supplementary structure has been minimized by using simple manufacturing techniques, keeping in mind that the amount of work to be done in the underground area has to be kept to a minimum, in particular heavy welding must be suppressed as far as possible.

The construction and assembly of the L3P yoke follows closely the construction solutions and assembly scenario successfully applied for L3. At both ends of the magnet, the already existing L3 octagonal crowns are used as self-supporting structures to take the weight of the roof of the magnetic barrel. These crowns consist of eight open frames filled with iron plates stacked side by side. The barrel, also recuperated from the L3 magnet, is constructed from individual steel bars arranged in an octagonal geometry. The three bottom octants, laying on an octagonally shaped concrete cradle, provide a foundation for the whole assembly, while the three top octants rest on the crown by their extremities. When L3P is closed, the central hole of the crown is filled with a movable pole plug. The new plug and the yoke are optimized for a maximum induction of 1.9 Tesla in the iron. The existing L3 doors, equipped with their toroidal winding, will be placed outside the new plug, to provide an additional measurement for the muons in the forward directions. The plug and the door together make the magnetic end-cap. This heavy magnetic end-cap can be displaced in the beam direction, on grease pads, to give access to the inner part of the magnet to load the superconducting solenoid system and the inner detectors, and later allow maintenance of the sub-detectors. The construction of the new plug is very similar to the construction of the present L3 doors. The grease pad system, foreseen to support the weight of the magnetic end cap, is a direct extrapolation of the one already used to support the 675 t L3 magnet doors and the 1,000 t L3 support tube. The weight is transmitted to the grease where the pressure reaches 500 bars and the friction factor is around 0.001. The moving mechanism is a step by step system which allows movement in 1 m steps.

For the 3 Tesla design option, an additional 50 cm thick iron layer will be necessary for the barrel, these will be provided by laying two 250 mm thick plates over the iron bars.

10

CHAPTER III
Central Tracking System

Outer superlayer

C

D

Beam

E

Align. reference

Inner superlayer
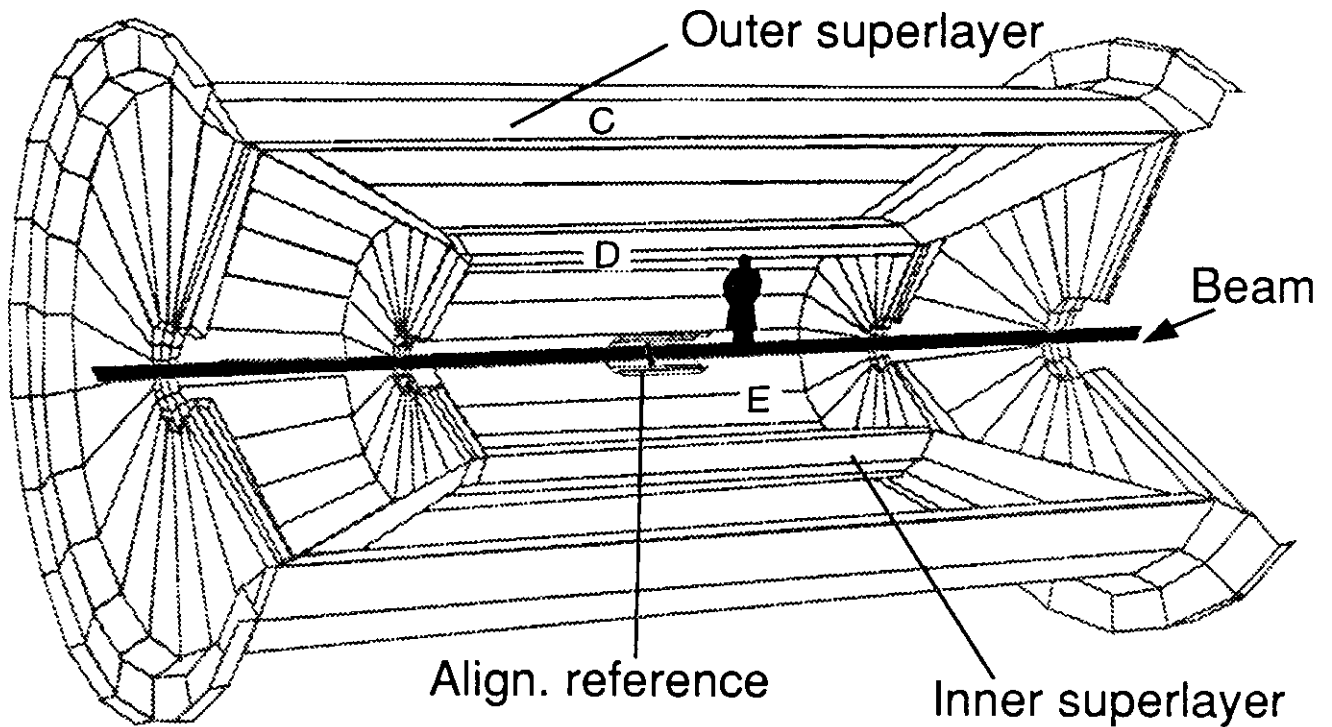
Figure 10   General view of Central Tracking System

Detector support frame
Carbon fiber Honeycomb
structure.

Proportional
Chambers

R = 2.7 m

Drift Tubes

Proportional
Chambers

R = 1.65 m

Z = 4.94 m   Z = 2.92 m

Alignment
reference
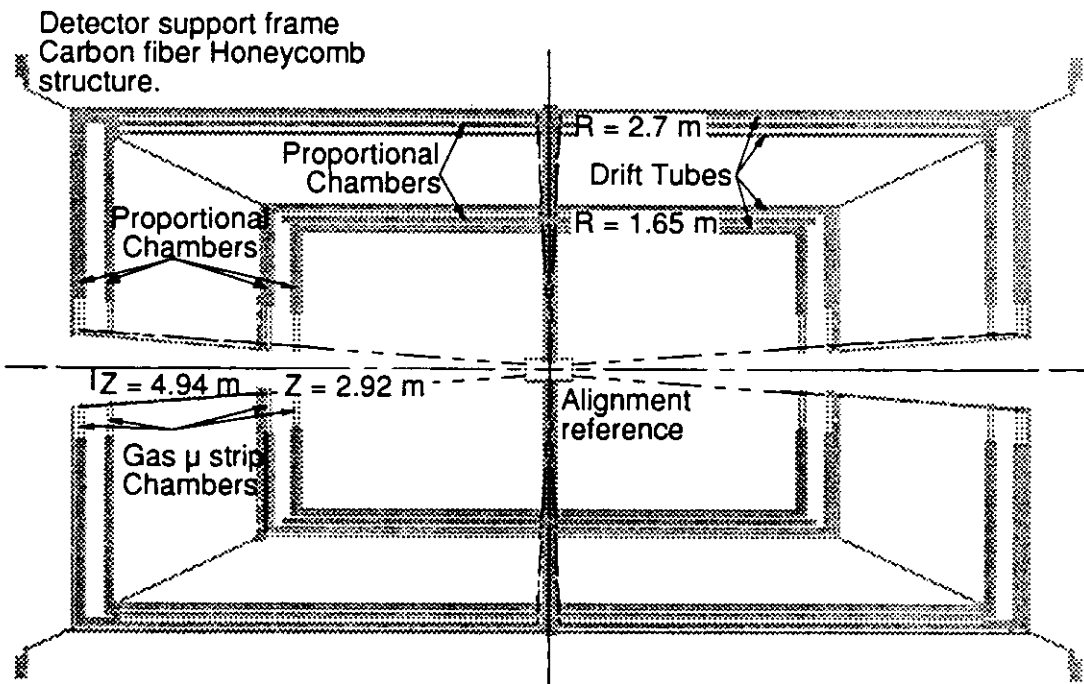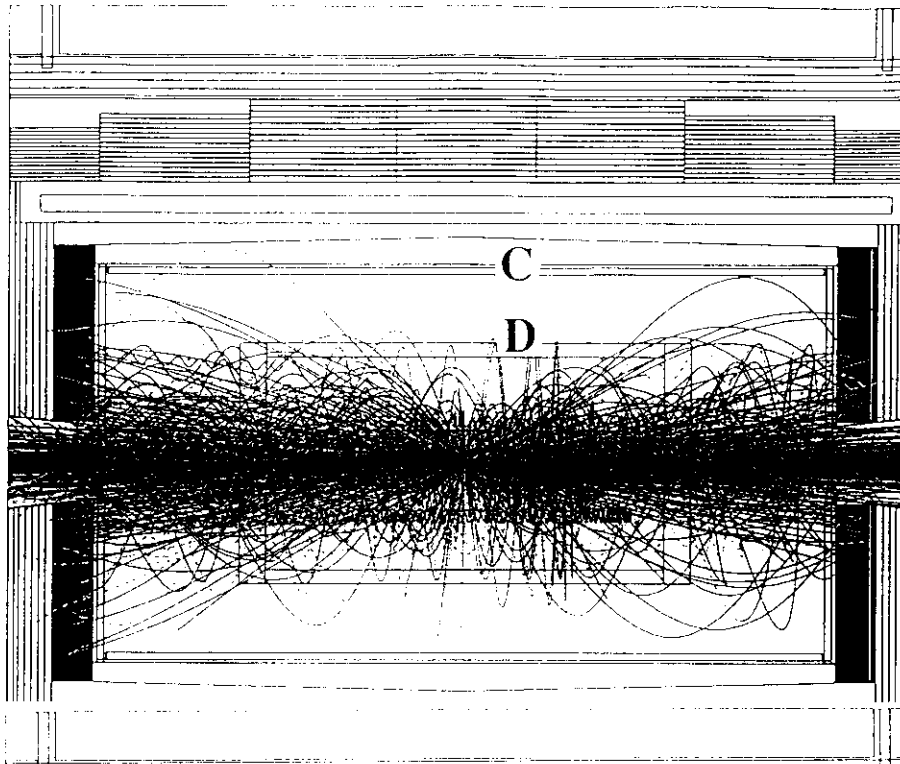
Gas μ strip
Chambers

Figure 11   Layout of the Central Tracking System

B = 2T　　　　**(a)**

B = 3T　　　　**(b)**
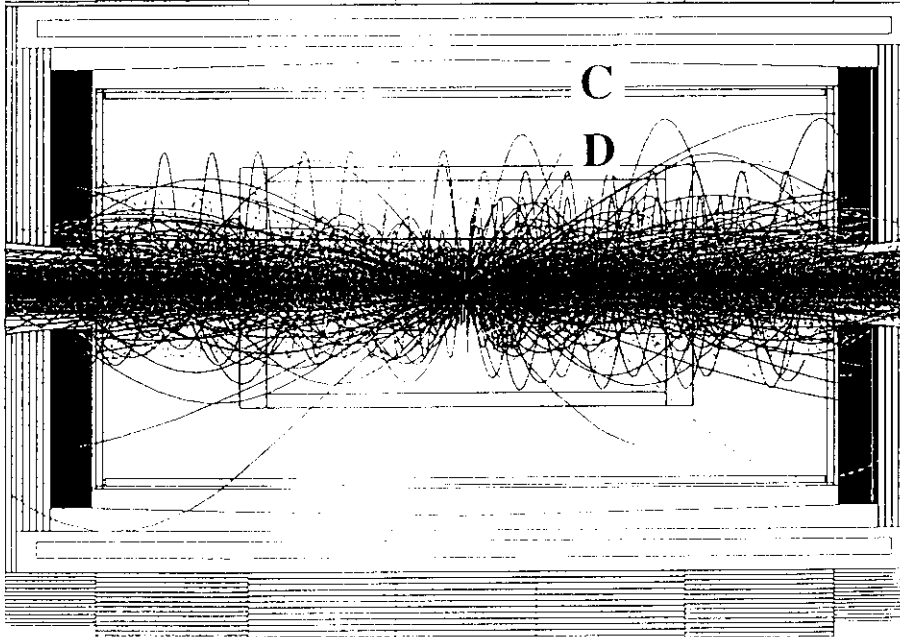
Figure 12: Charged particle tracks from 12 minimum bias events corresponding to one bunch crossing at $\mathcal{L} = 10^{34} cm^{-2} s^{-1}$; a) in the 2 T field, b) in the 3 T field.

3. CENTRAL TRACKING SYSTEM

3.1. Introduction

The layout of the central tracker system is shown in Fig. 1, Fig. 10, and Fig. 11. It consists of a barrel covering $|\eta| \leq 1.4$ and a forward tracker at $1.4 \leq |\eta| \leq 3.0$. In accordance with the discussion on design considerations presented in chapter 1.3, this central detector is designed to have the following properties:

- It provides a resolution:

  $\Delta p/p = 1\%$ at $p_t = 100~GeV/c$ at $2~T$,
  $\Delta p/p = 0.7\%$ at $p_t = 100~GeV$ at $3~T$.
  $\Delta p/p = 0.36\%$ at $p_t = 100~GeV$ with the final system (see Chapter 12).

- It contains a total of $0.03~X_0$ of material in order to minimize photon conversion and to avoid degrading the resolution of the electromagnetic crystals.

- The first detector is 1.65 meters away from the beam line, thus it is not reached by most background particles, which are restricted to a lower radius by the magnetic field.

- The tracker is designed to operate at the maximum luminosity of $\mathcal{L} = 4 \times 10^{34}~cm^{-2}~s^{-1}$ with the possible exception of the very forward region.

- The entire tracker ($260~m^3$) can be removed and a new tracker can be installed for specialized physics research, such as heavy ion physics.

Figs. 12a and b show particles arising from a single bunch crossing (at $\mathcal{L} = 10^{34}~cm^{-2}~s^{-1}$) in the L3P detector for two field values(2T and 3 T). The major detector background is due to low-p_t charged particles produced in "minimum bias" interactions (Fig. 13). The magnetic field curls the trajectories of these particles, which can induce multiple hits in the trackers (Figs. 12a and b). Because the background is considerably higher at small θ (see Fig. 14), different detector technologies are specified for the barrel and forward regions, as described below.

3.2. Barrel Tracker

The barrel spans the rapidity range $|\eta| \leq 1.4$ (see Fig. 11). The barrel initial tracker is shown in
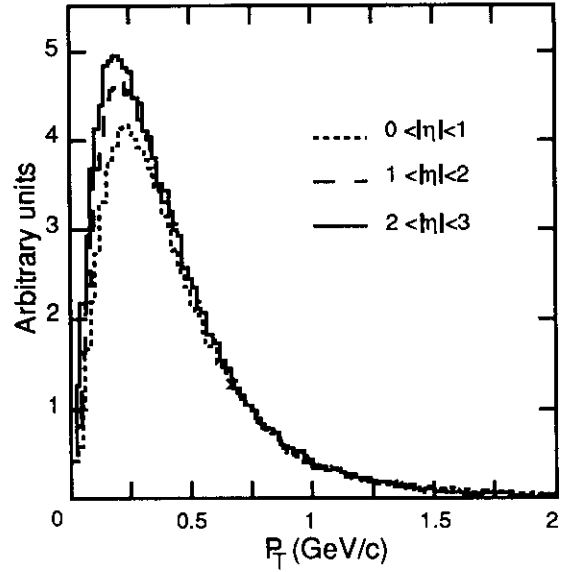

Figure 13: p_t of minimum bias event particles in different rapidity ranges.
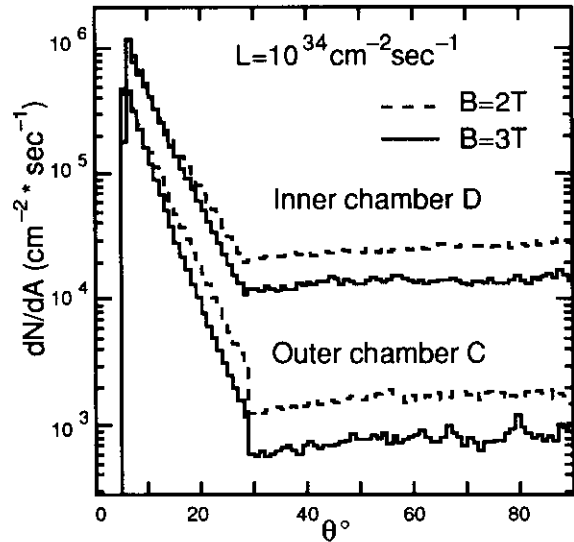

Figure 14: Background rate in different regions of central tracker. For the central region the 3 T field will reduce the rate by a factor of 2.2.

Fig. 15 and the final design is discussed in Chapter 12. The tracker is used to determine the momenta of charged tracks originating at the interaction point (IP) by measuring their sagitta in two concentric superlayers composed of drift tubes and proportional chambers.

High coordinate accuracy is needed in the bending (r/ϕ) plane in order to obtain a precision momentum measurement. This accuracy is achieved by sampling the track position at several measurement planes within the two superlayers. By measuring the bending coordinate N times, the average measurement improves in accuracy by a factor of $\sqrt{N}$; this multisampling technique has been successfully applied in the muon chambers of the L3 experiment [15].

The two barrel superlayers are located at average radii of 1.65 m and 2.7 m. Although the most sensitive momentum determination is achieved when the three measurement sites are equally spaced, the inner superlayer (which effectively measures the sagitta of a track between the IP and the outer layer) is displaced to a slightly larger radius. This is done to gain a considerable background reduction (i.e. a factor 1.5) with less than 4% change in the momentum precision.

The inner superlayer, at R = 1.65 m, performs a precise coordinate measurement using 8 planes of drift (straw) tubes [20], which are grouped into two clusters (each 4 tubes deep), separated radially by 20 cm.

The radial separation within a superlayer introduces a local lever arm that helps in rejecting background tracks, which are mainly at low p_t (Fig. 13), thus curl significantly in the magnetic field (Figs. 12a and b). In contrast, the high momentum particles from the events of interest have almost straight trajectories, hence they are better distinguished (see Fig. 15).

The straw tubes are made out of thin (25 μm) plastic-wall tubes with a diameter of 5 mm. The tubes contain a $CF_4 + Ar + isoC_4H_{10}$ gas mixture and operate in the proportional mode. This gas mixture is chosen because it has a large electron drift velocity (100 μm/ns). This property provides a fast (drift+shaping time < 45 ns) coordinate measurement in each tube with an accuracy of 125 μm [21].

A measurement in the the inner superlayer (containing 8 layers of straw tubes) thus provides an accuracy $\sigma = 125\mu m/\sqrt{8} \approx 45\mu m$. The length of the straw tubes is limited by the maximum occu-

pancy ($\sim$ 1%) that can be tolerated without significant loss of reconstruction efficiency. Accordingly, the inner superlayer tubes are each 30 cm long.

In order to aid pattern recognition in the tracker barrel, a set of proportional chambers are sandwiched between the two layers of drift tubes. Three successive planes of these chambers are at 0°, 120°, and -120°, which causes a legitimate particle track to produce signals on a triplet of wires. The distances d_1, d_2, d_3 measured from the 3 wire plane satisfy the relation

$$d_1 + d_2 + d_3 = const.$$

A fast validity check can then be performed (i.e. the wires hit in the first two chamber planes uniquely determine the wire that must fire in the third, such that all three wire addresses always sum to the same constant), thereby resolving ambiguities that can be expected from neutron albedo and a noisy, high-rate environment. Chambers of this type were successfully used to resolve high-background, multi-track events in experiments ran at luminosities above $10^{36}cm^{-2}s^{-1}$[2].

To keep material at a minimum, these pattern recognition chambers are supported on very large thin frames, see Fig. 16a, and possess on-chamber sparsification electronics that reduce the required cabling bulk by at least a factor of 16. The compressive force of the wires is supported by Rohacell planes (0.05 g/cc) with inlayed C-fiber supports. The 0^0 plane is segmented into 1 meter long overlapping sections, see Fig. 16b. The frames of the large modules also overlap in $r\phi$, in order to attain full acceptance.

These chambers are filled with the same gas mixture used by the drift tubes. The introduction of CF_4 is known to lower the aging rate of gas detectors [22]. This is an important feature, considering the large (and somewhat unpredictable) background rates expected at LHC.

The outer (at R=2.7 m) and inner superlayers have similar structure. The outer superlayer, however, contains 4 layers of drift tubes, thus producing a net bending-plane coordinate measurement of $\sigma = 125\mu m/\sqrt{4} \approx 62\mu m$.

Since the background expected in the outer tracker is about a factor of 10 lower than that of the inner tracker (see Fig. 14), the length of the anode wires in both the drift tubes and proportional chambers can be increased from 30 cm to 1 m, and the anode wire pitch in the proportional chambers coarsened from 1.5 mm to 3 mm.

As indicated above, the measurement of particle momenta can be degraded by multiple scattering in the tracker structure. Excessive material in the tracker region can also create additional charged background by converting photons arising from π^0 decays. In order to address these concerns, provisions are taken to minimize the amount of material used in the mechanical structure of the trackers. Accordingly, the thin plastic walls of all drift tubes and proportional chambers of the central tracker are designed to introduce as little as 0.03 X_0.

A special R&D program is dedicated to minimizing the material needed to supply the gas and anchor the wires.

The main features of the barrel tracker are summarized in Table 5.

3.3. Forward Trackers

Forward (backward) trackers (Fig. 11) cover the rapidity range $1.4 \leq |\eta| \leq 3.0$. As in the barrel, charged particle momenta are determined by a sagitta measurement. Because of the projection into the bending plane, particles passing the forward detectors will have a lever arm $(\ell_\perp)$ that decreases with polar angle θ (as opposed to the barrel arrangement, which results in a $\ell_\perp$ independent of θ). The two forward tracker superlayers are situated along the beam axis, at 3 m and 5 m from both sides of the interaction point.

A forward superlayer consists of several proportional chamber planes in combination with μ-strip gas chambers (MSGC) [23] installed at small angles. These components are grouped into two sublayers of similar structure. A schematic of such a sublayer is shown in Fig. 17.

The forward chamber arrays are designed as a series of disks centered on the beamline, with anode wires stretched in the radial direction. Fig. 17 portrays slices of these disks as arranged in a sublayer (the disks are also radially segmented, as will be discussed below). A superlayer is composed of 2 sublayers, each of which contains 4 disks. Successive disks in a sublayer are rotated about the beam axis (relative to their predecessor) through an angle that displaces the corresponding wires in neighbouring disks by 1/4 of their ϕ pitch. This staggered arrangement of chamber disks produces an effective sublayer position resolution that is a factor of 4 better than that achieved with a single chamber. The superlayer arrangement thus achieves a net coordinate resolution of: $\left(\frac{sector-width}{\sqrt{12}\times 4}\right)$.

The anticipated flux of charged particles through the forward trackers is plotted as a function of radius in Fig. 18a (for the inner superlayer) and Fig. 18b (for the outer superlayer). The chambers spanning the tracker disks are radially segmented into concentric annular regions, to maintain a low occupancy and to keep a close wire spacing (hence preserving the measurement granularity). According to the expected background flux at the chamber location, a tracker disk is divided in up to four such annuli, which are labeled as regions 1-4 in Figs. 17-18b. Proportional chambers cover the regions at larger radius; the wires are spaced such that their minimum separation is 2 mm. The disks composing the superlayer closest to the IP (situated at 3 meters along the beam axis) contain two annular regions of proportional chambers (regions 3,4; see Figs. 17 & 18a). The superlayer at larger distance (5 meters along the beam axis) is composed of disks split into 3 such annular proportional chambers (regions 2,3,4 in Fig. 18b).

The segments of the forward tracker closest to the beam consist of MSGC's (regions 1 and 2 in Figs. 17 & 18a, and region 1 in Fig. 18b), with radially-directed strips pitched at a 0.2 mm minimum width. There is one such layer of MSGC contained in each sublayer of the forward trackers (thus the MSGCs appear in only one of the disks portrayed in Fig. 17).

To measure the radial track coordinates and facilitate pattern recognition, each sublayer is complemented with two additional proportional chambers, having anode wires at $\pm 120^0$ (these are shown at left in Fig. 17).

As in the barrel trackers, a fast, low aging-rate gas mixture of $CF_4 + Ar + isoC_4H_{10}$ is used in all of the forward chambers.

The measurement accuracy of the forward system will be $\sim 100\mu$m at larger angle (where measured by radial proportional chambers) and $\sim 40\mu$m near the beamline (where measured by MSGC's). The parameters of the forward tracking system are listed in Table 6.

3.4. Mechanical Accuracy and Alignment

The large volume of the L3P inner tracker, together with its low density (thus extremely small multiple scattering) enable a high-precision momentum measurement to be performed. As outlined in the example given below, a resolution of $\Delta p/p \leq 1\%$ can be achieved at $p = 100\ GeV$, provided the mechanical accuracy is known to $\Delta x = 30\mu$m.

Table 5: Parameters of the barrel central tracker

	Inner superlayer	Outer superlayer
Total length [m]	6	9.8
Radius of first drift tube layer [m]	1.55	2.6
Radius of second drift tube layer [m]	1.75	2.8
Length of drift tubes [m]	0.3	1.0
Occupancy/(tube × bunch) at $10^{34} cm^{-2} s^{-1}$	0.006	0.0009
Number of layers in drift tube layer	4	2
Measurement accuracy in the bending plane [μm]	45	62
Total number of drift tubes (TDC channels)	331,752	135,717
Radius of proportional chamber layer [m]	1.65	2.7
Length of proportional chamber wires [m]	0.3	1.0
Total number of proportional chamber wires (Digital channels)	229,940	166,430

The trajectory of a 1 TeV muon in a B=2T field over $\ell_\perp = 2.8$ m will produce a sagitta of:

$$s = 0.3 \text{ B } \ell_\perp{}^2/(8 \ p_t) \approx 600 \ \mu m$$

Scaling from 1% at 100 GeV, the expected resolution becomes $\Delta p/p = \Delta s/s = 10\%$, implying that $\Delta s = \sqrt{\delta^2 + (\Delta x)^2} \leq 60\mu$m, where $\delta = 53$ μm is the resolution of a multi-chamber superlayer. Consequently, we obtain as requirement on the mechanical accuracy: $\Delta x < 30\mu$m.

For a 3 T field the same alignment accuracy is necessary to improve the resolution at higher momenta. In order to achieve the ultimate resolution of $\Delta p/p = 0.36$ % at p = 100 GeV, the r.m.s. mechanical alignment error should be: $\Delta x \leq 20\mu$m.

This is a very tight alignment tolerance, which demands:

- A carefully designed and highly reproducible support structure, with accurately predictable deflections under load.

- Special instrumentation for high-accuracy initial survey and alignment.

- Dynamic monitors that precisely record subsequent deviations caused by temperature, pressure, magnetic field, and other environmental changes.

In L3 we have reached such accuracies in a volume of more than $1,000 m^3$. At L3P we note two essential advantages that will aid significantly in attaining a 20 μm alignment:

- The inner volume is a large open space, allowing unobstructed alignment lines-of-sight and a monolithic support structure.

- The structure is light and thermally stable.

- Application of previous L3 experience and precision instrumentation.

Indeed, accuracies of $< 30\mu$m were achieved in all 16 modules of the L3 muon detector [15] (see Fig. 19). Set to "0" by optomechanical systems, the alignment was independently verified by cosmic rays and UV lasers. The r.m.s. of the measured sagittas is indeed

$$\Delta x = 17\mu m.$$

This has been verified by measuring the momentum resolution in $Z \to \mu^+\mu^-$ decays (see Fig. 20).

The total volume of the L3 muon system is 1,000 m^3. It is divided into 16 modules, each of which has a volume of (6 x 6 x 3) m^3 and weighs 5.8 tons (the entire L3P central tracker is thus comparable in size and volume to a single L3 muon module). The middle plot of Fig. 21 shows the measured deflection at the most sensitive spot of a L3 module under a 360° rotation, during which the structure reproduced to within the measuring accuracy of 6 μm.

The L3 octants track the position of the three precision chamber layers that measure the sagitta (i.e. momentum) with specially developped and inexpensive "straightness monitors" [24], which are depicted in Fig. 21. Light from an LED mounted

Table 6: Parameters of the forward central tracker

	First superlayer	Second superlayer
Distance from interaction point [m]	3	5
Radial span of MWPC's [m]		
1	0.8-1.1	0.9-1.2
2	1.1-1.7	1.2-2.0
3		2.0-2.8
Number of layers of MWPC's		
Chambers with staggered ϕ pitch	4×2	4×2
Pattern recognition chambers	2×2	2×2
MWPC measurement accuracy in the bending plane [μm]	100	100
Number of channels in MWPC's		
1	31,200	30,000
2	42,000	46,800
3		75,600
Total on both sides	146,400	304,000
Occupancy/(MWPC channel $\times$ bunch) at $10^{34} cm^{-2} s^{-1}$ [%]		
1	1.5	1.8
2	0.8	0.8
3		0.2
Radial span of MSGC's [m]		
1	0.32-0.5	0.52-0.9
2	0.5-0.8	
Number of layers of MSGC's		
	1×2	1×2
Number of channels in MSGC's		
1	20,000	34,000
2	32,000	
Total on both sides	104,00	68,000
Occupancy/(MSGC channel $\times$ bunch) at $1 \times 10^{34} cm^{-2} s^{-1}$ [%]		
1	0.5	0.3
2	0.3	
MSGC measurement accuracy in the bending plane [μm]	40	40
Total number of channels (Digital readout)	250,400	372,800

μ

C

R = 2.7 m

2 Drift Tubes
125 μ / √2

0°
120°
-120°

Prop. Chamber
3 mm / √18

2 Drift Tubes
125 μ / √2

D

R = 1.65 m

0°
120°
-120°

4 Drift Tubes
125 μ / √4

Prop. Chamber
1.5 mm / √18

4 Drift Tubes
125 μ / √4

E

IP   R = 0
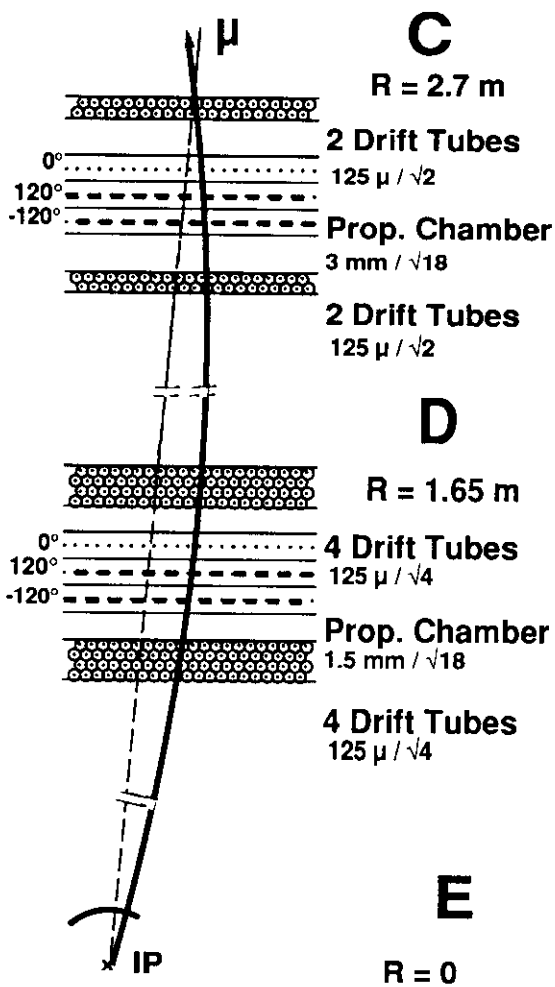
Figure 15: Layout of barrel trackers.
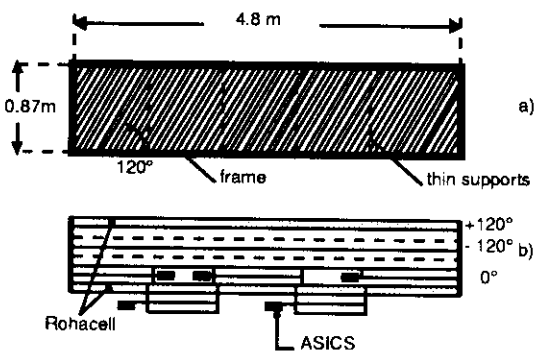
Figure 16: Pattern recognition chamber installed in the outer barrel layer.

Proportional
Chambers   Radial
                                     Proportional
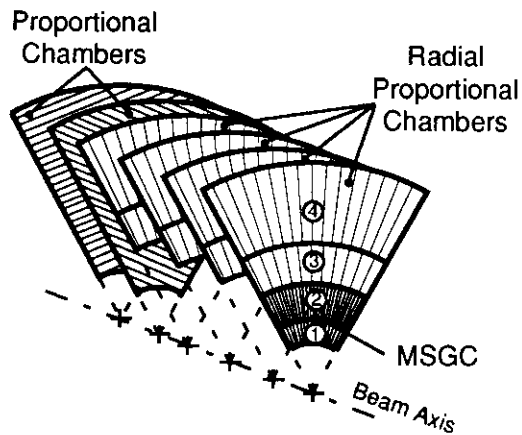   Chambers

MSGC

Beam Axis

Figure 17: Schematics of forward tracker sublayer.

on layer 1 is projected through a lens on layer 2 onto a quadrant diode on layer 3. As calibrated on an optical bench, these points align perfectly when all quadrants receive equal light. When installed on the chambers, the detected illumination imbalance thus provides a precise measure of the 3-point misalignment. The bottom plot of Fig. 21 shows the behaviour of a L3 module over 2 years of running, as measured by these monitors. Better than 10 μm absolute and 5 μm relative accuracies were maintained.

Figs. 22 and 23 show the L3P tracker being supported by a carbon fiber structure with honeycomb cylinders. The entire detector is light (i.e. 3 tons, half of the L3 module weight). Similar straightness monitors are used to align the superlayers to one-another and the IP, as schematically depicted in Fig. 23. The technologies developed at L3 will thus be adequate for attaining the required 20 μm mechanical alignment.

The tracker structure is self-contained and internally aligned. The tracker is suspended from the calorimeter and adjusted by 3 kinematic mounts at each end. Straightness monitor components are mounted on the two superlayers (photodiode on the outer and lens on the inner). A small, lightweight cylinder at the center of the tracker (termed the "alignment reference" in Fig. 23) carries radiation-hard light sources that illuminate the straightness monitors, which are between the corners of the fiducial volume at the edges of superlayer boundaries (as depicted by dotted lines in Fig. 23). This cylin-
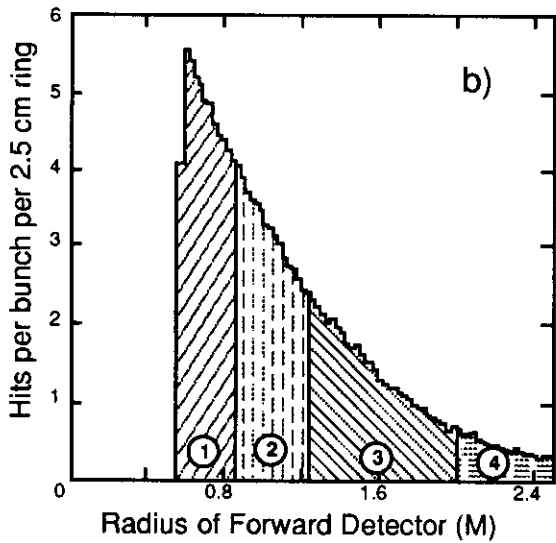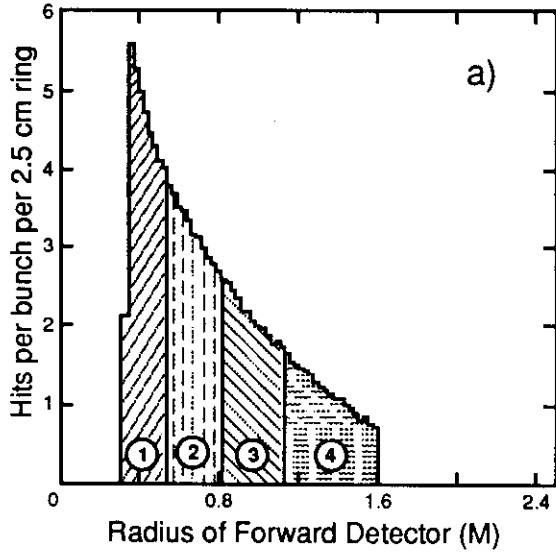
a)

b)

Figure 18: a)Dependence of background in the forward tracker at 3 m, b) dependence of background in the forward tracker at 5 m.
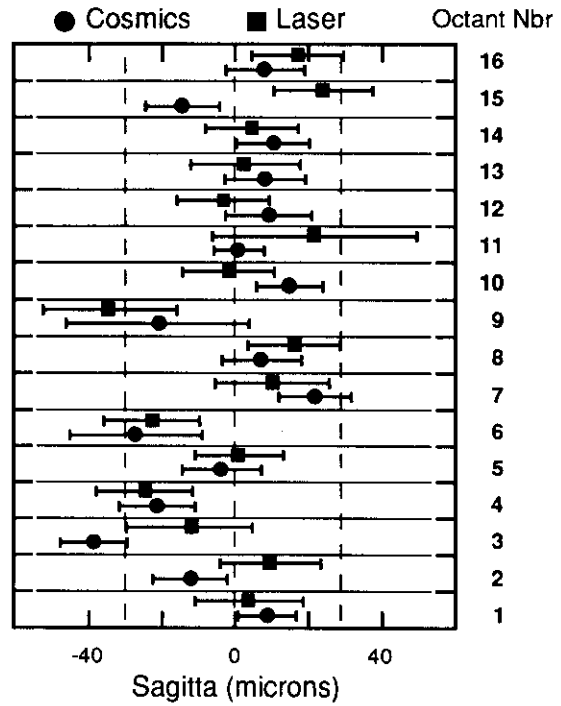

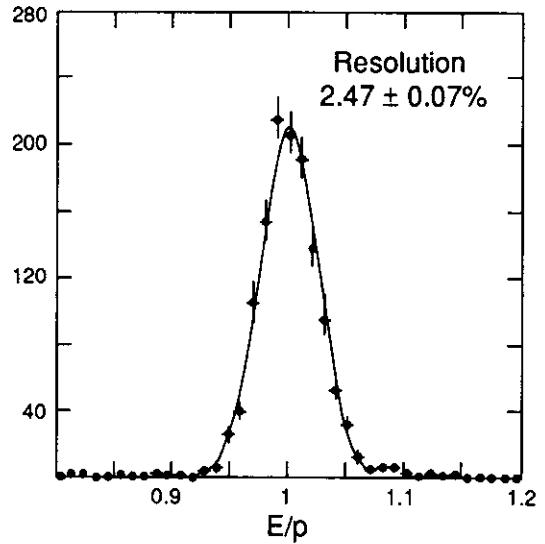Figure 19: Alignment results for all 16 L3 octants.

Figure 20: Momentum Resolution for $Z \rightarrow \mu^+\mu^-$ at L3.
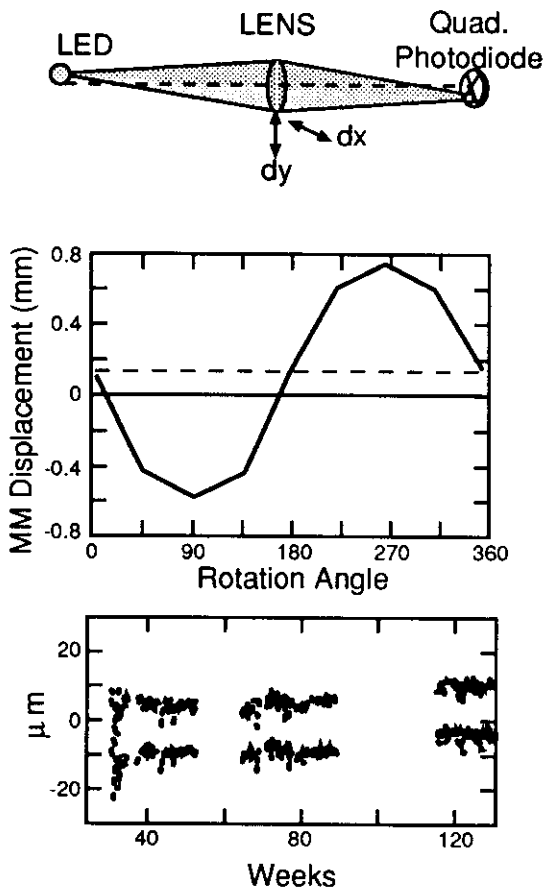
18

Figure 21: The L3 alignment system: L3 Straightness Monitor (top), Measured and calculated deflection during $0^\circ - 360^\circ$ rotation (middle), Alignment accuracy over 2 years of operation at L3 (bottom).

der is in turn located relative to the beam pipe (by which the interaction point is determined) by touchless proximity sensors. If the beam tube is not sufficiently stable, the beam reference can be acquired by inserting additional monitors that track the machine quadrupoles. The beam can also be more directly located with respect to the reference cylinder by using beam position monitors (i.e. pickup electrodes or flux loops fixed to the beam tube). The precision calibration of such devices and their operation in the strong magnetic field will require additional R&D.

The entire tracker thus forms a closed system, with only one "global" reference required from the outside. The forward, barrel-left, barrel-right, and backward modules are attached to a common structure, and are independently aligned by straightness monitors. Since a precision of $20\mu m$ is required from the sagitta measurement, the straightness monitor elements are referenced directly to the precision-machined end plates that locate the drift tube sense wires, thereby incurring minimal alignment transfer error.

Fig. 22 shows an end-view of the chambers, as mounted in concentric support cylinders that are held in position by cross-braced tension rods. Besides resulting in a light structure, this mounting strategy exclusively applies linear forces, insuring that the structure can be reliably modelled (as was accomplished at L3 [15]). This is not possible if plates and welds introduce additional tensor forces that can change with temperature gradients. For thermal stability, carbon fiber materials (< 3 ppm/$^\circ$C) are used, which have a low radiation length, yet maintain high strength.

To avoid induction shocks from changes in the magnetic field, the support cylinders are longitudinally interrupted by an insulating strip.

3.5. Readout Electronics

The initial data acquisition system will accept timing information from about 500k drift tubes for time-to-digital conversion and about 1,000k channels of digital (binary) information from proportional chambers and MSGC's (see Table 7).

Because of the high channel count, we are planning to site much of the electronics at or near the detector (i.e. certainly the preamplifier/discriminator/sparsification ASICs, and possibly the drift tube TDCs & digital pipelines as well).

The drift tube TDCs (Fig. 24) will measure the drift time relative to the most recent beam crossing

19

with a 1 ns resolution. Accordingly, only 4 bits of
TDC range are required to span the full 15 ns bunch
crossing period. The TDC output is sampled by a
5-bit digital pipeline, clocked synchronously with
the beam gate (four bits are used for the drift time
information, with an additional bit to signal the
hit occurance). The digital pipeline is planned to
be 128 locations deep, allowing a first level trigger
decision delay of 2 μs. Upon receiving a first level
trigger, the contents of the pipeline location corre-
sponding to the accepted event (plus the contents
of the 3 previous stages) are transferred to a local
buffer and propagated through the readout chain.
In this fashion, the 60 ns history following trigger
signal, i.e. the whole range of the straw tube drift
time, will be available for subsequent analysis.

Similar readout electronics will be used for both
the proportional chambers and gas micro-strip de-
tectors (see Fig. 25). Since time information is not
produced, these channels will not contain TDCs,
hence their digital pipeline will be only 1-bit wide.
Only a single pipeline location needs to be trans-
ferred upon receipt of a level 1 trigger, if the pro-
portional chamber signals arrive within a single
beam gate (otherwise previous pipeline locations
must also be included).

3.6. Performance
3.6.1. Momentum Resolution
As previously discussed, the central tracker pro-
duces a momentum measurement that is derived
from the track sagitta determined from the two su-
perlayers. This approach requires that the interac-
tion point is known to $20\mu m$ RMS in the bending
plane and to 5.7 cm RMS along the beam axis.

The momentum resolution of the central tracking
system is shown in Fig. 26 for 100 GeV particles.

3.6.2. Pattern Recognition
The $\sim$ 45 ns latency of the drift tubes is sig-
nificantly longer than the 15 ns bunch-crossing pe-
riod at LHC. As a result, background from several
bunch crossings (see Figs. 12a and b) will superim-
pose, correspondingly increasing the effective oc-
cupancy of the inner trackers. Moreover, since the
rotation period of spiraling background particles is
rather long (30 - 60 ns per cycle), particles from
previous bunch crossings will contribute to the in-
stantaneous background included with the recon-
structed event (this effect has been accounted for
in Fig. 14).

We have performed a Monte Carlo [25],[26] study
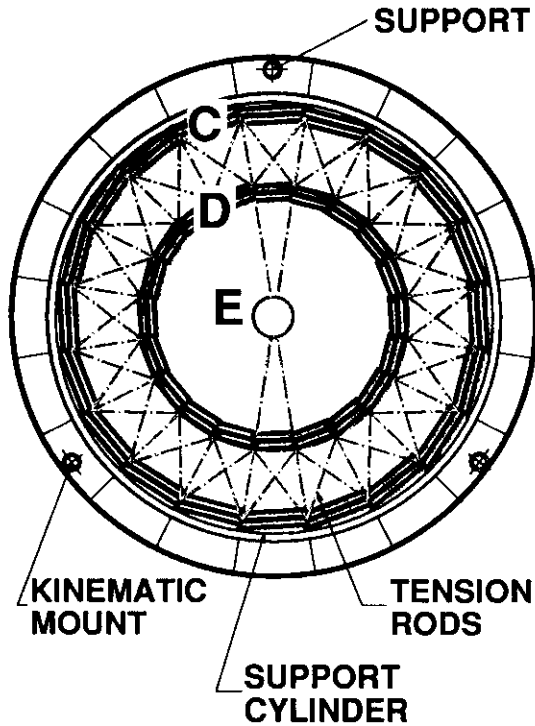
Figure 22: End view of central trackers showing
the support structure.
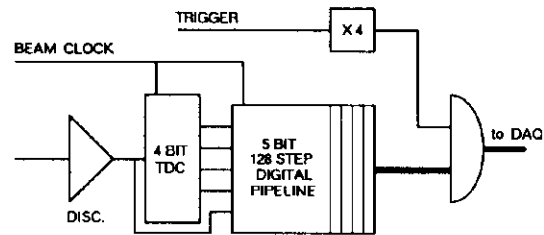
Figure 24: Readout channel for time measure-
ments.

20

Table 7: Associated Electronics Requirements.

	Signal	Resolution	Dynamic	Electronics	Nb. of channels
Straw Drift Tubes	Timing	1 ns	60 ns	Disc., TDC	500k
Prop. Chambers	Hit	15 ns		Disc.	1,000k
Gas Micro-Strip	Hit	15 ns		Disc.	200k

Figure 23: Mechanical structure of central trackers; elements of the alignment system are shown.

Figure 25: Readout channel for proportional chambers.

Pattern recognition efficiency

Figure 27: Muon momentum reconstruction efficiency at different momenta in barrel trackers for a 2 T coil. Note, for a 3 T coil the reconstruction efficiency is very close to 100%

to examine the efficiency of the momentum reconstruction in the central tracking system for isolated charged particles (i.e. leptons produced in processes such as $H^0 \to Z^0 Z^0 \to 4l$ or heavy gauge boson decays like $Z' \to l^+ l^-$).
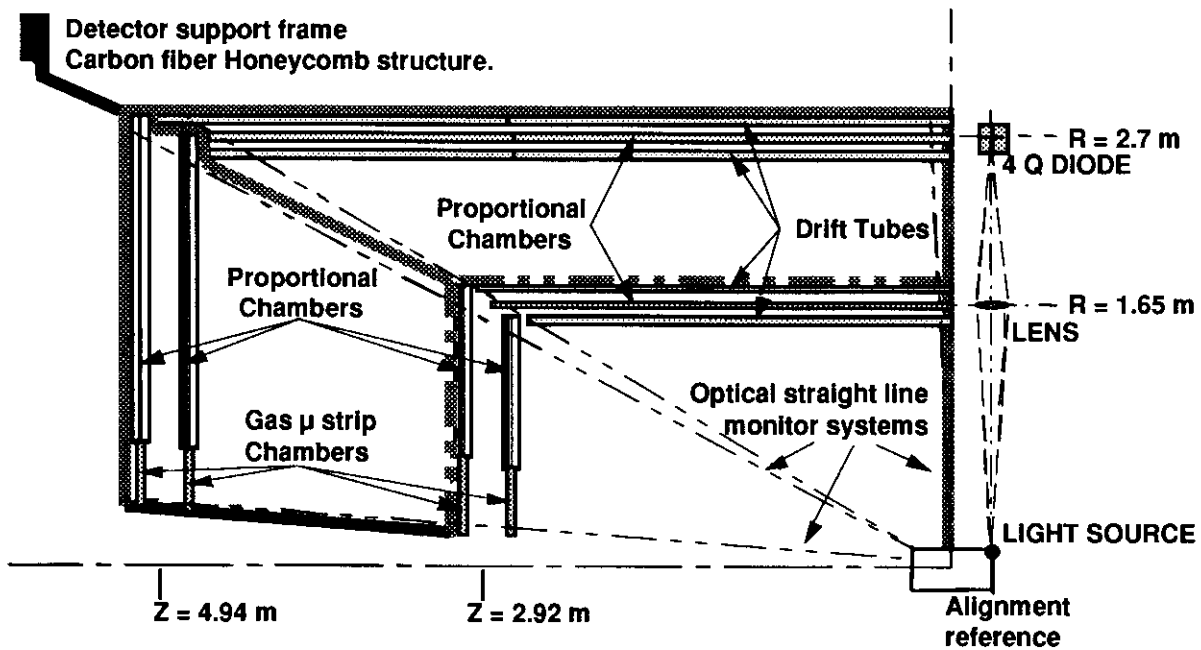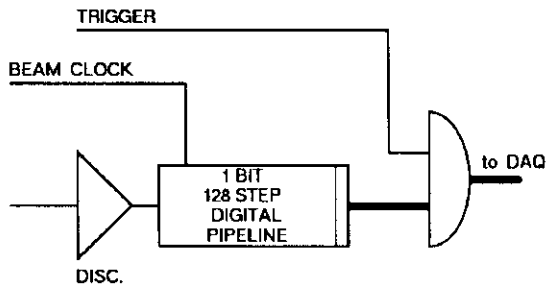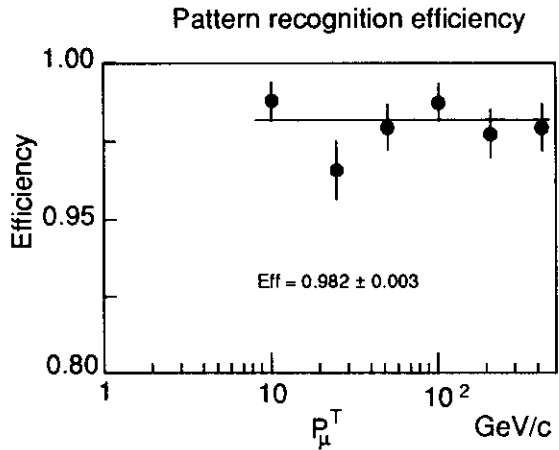
The leptons were reconstructed in the presence of "minimum bias" background corresponding to 5 superimposed bunch crossings (75 ns) at a luminosity of $10^{34} cm^{-2} s^{-1}$.

An important part of the pattern recognition and analysis will incorporate the information from other L3P subdetector systems. For example, reconstruction of an electron relies on matching the position and energy of a shower measured in the high-granularity electromagnetic calorimeter (see Chapter 4) with the direction and momentum of a particle track measured in the central tracker, which will provide an accurate measurement ($\sim$ 1 mm) of the impact coordinates.

Muon momenta are independently measured in the muon system (see Chapter 6). In the barrel region of the central tracker, a muon reconstuction algorithm uses the measurements of the background-free outer muon system (which estimates the momentum with $\sim$ 14% accuracy for a 2 T coil) to identify the locations of candidate muons in the central tracker.

This information defines a fiducial zone in the inner tracking system within which the muon track must appear. Combining the corresponding tracker data with the muon system measurements (see A,B in Fig. 1) we can obtain a $\sim$ 6% momentum accuracy using the outer superlayer of the inner tracker (C) for a 2 T coil and $\sim$ 4% for a 3 T coil. The final resolution of $\sim$ 1% at 100 GeV for a 2 T coil

and $\sim$ 0.7% for a 3 T coil is obtained when incorporating data from the inner superlayer (D). A momentum reconstruction efficiency close to 100% is reached for muons traversing the barrel region (Fig. 27).

Fig. 28 shows the reconstructed muon resolution at 100 GeV wit h and without a 60-event minimum bias background, plotted for $|\eta| \leq 3$. Fig. 29 shows the corresponding track reconstruction efficiency. Both the resolution and efficiency in the forward regions ($1.4 \leq |\eta| \leq 3$) are different from those in the central region ($\eta \leq 1.4$) because of the of high background density.

3.7. R&D Program

- An investigation of the mass production of accurate drift tubes has been started ($\sim$ 500K such devices will be needed for L3P). Prototype tubes of 25 μm wall thickness, 5 mm diameter, and 1 meter length have been constructed at ETH Zurich. Particular attention is given to reducing the material introduced through gas and electrical connections.

- A corresponding study of suitable drift gases at MIT has measured drift velocities and examined the behavior of several candidate mixtures, leading to the choice of $Ar : CF_4 : isoC_4H_{10}$; see Fig. 30. Additional tests
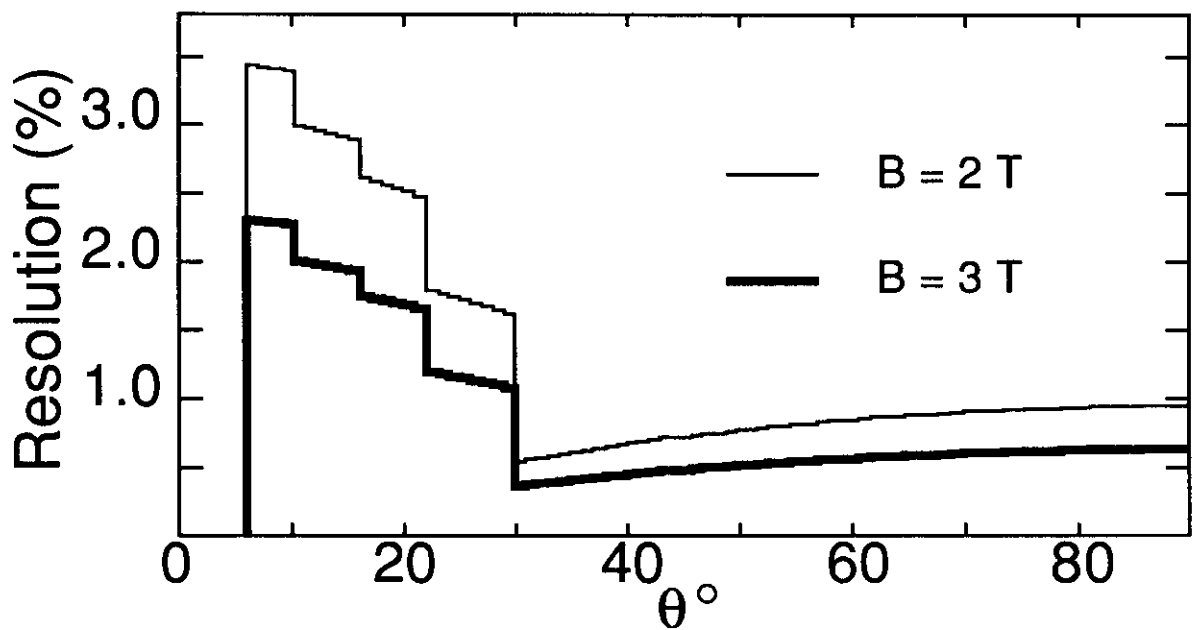
22

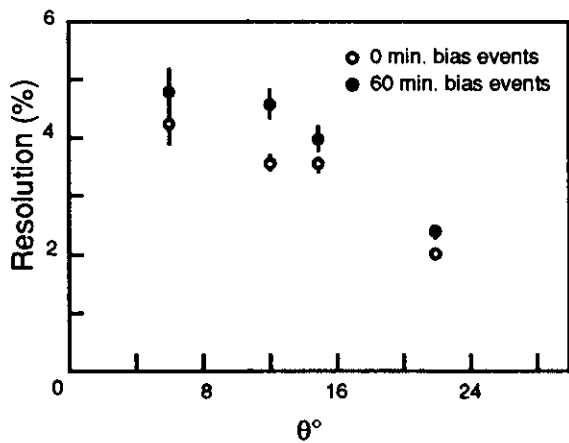Figure 26: Central tracking system momentum resolution at 100 GeV.

Figure 28: Accuracy of 100 GeV muon momentum measurement in the forward trackers for a 2 T coil. For a 3 T coil the resolution improves approximately by a factor of 1.5.
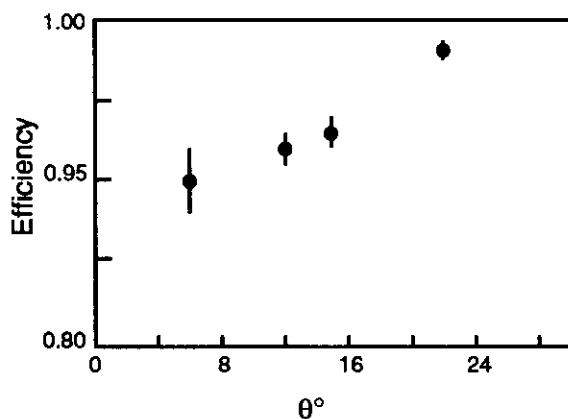
Figure 29: 100 GeV muon momentum reconstruction efficiency in the forward trackers. The efficiency does not change from 2 T coil to a 3 T coil.

23
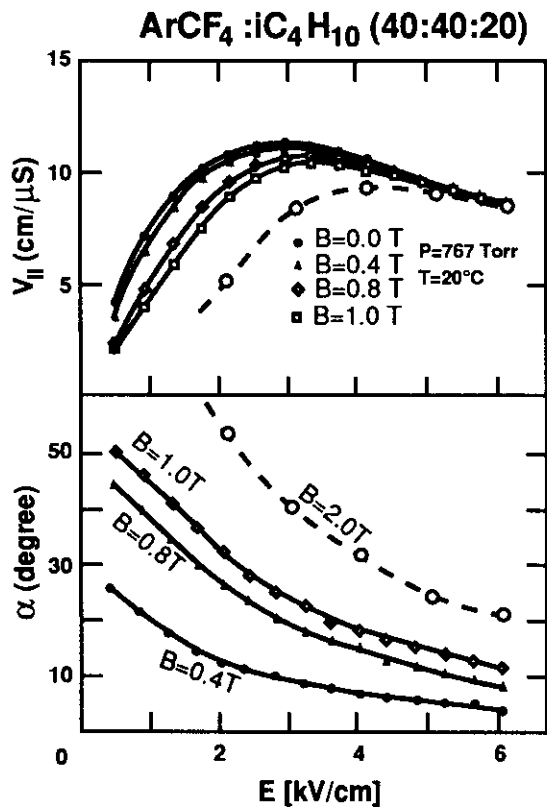
Figure 30: Measured characteristics of candidate gas mixture. The B = 2.0 T curve is based on calculations.

are underway to determine the exact time-distance relationship, and to optimize the gas performance at higher magnetic fields.

- Designs of the tracker structure must be evaluated. Accordingly, they will be modelled and analyzed via the NASTRAN software package. This procedure was used for L3 and produces estimates of the static, dynamic and thermal structural response.

- Although the straightness monitors present now a sufficiently mature technology for our applications, appropriate proximity sensors and beam position monitors must be searched for.

- Cost-effective production of proportional chambers with Rohacell carriers are being studied and prototypes are under design. The chambers will be tested for their long-term stability. Simple techniques of mounting the readout ASICs are being studied. The behavior of these chambers with the CF_4 gas used in the drift tubes is being investigated.

- Low-cost, radiation-hard electronics for chamber readout and data processing is under study by ETH Zurich and LeCroy Research, Geneva.

- Gas microstrip chambers will be investigated with CF_4-based gases in a magnetic field.

24

CHAPTER IV

Electromagnetic Calorimeter

Figure 31. Electromagnetic Calorimeter division

Figure 32. Mass spectra of π°, Σ°, η° as measured in L3 BGO Calorimeter

4. ELECTROMAGNETIC CALORIMETER

4.1. Introduction

The design principle of the electromagnetic calorimeter is based on the practical experience derived from the construction and operation of the L3 BGO crystal calorimeter [15] and many years of precisely studying electrons and photons at high intensity beams. The L3P electromagnetic calorimeter system in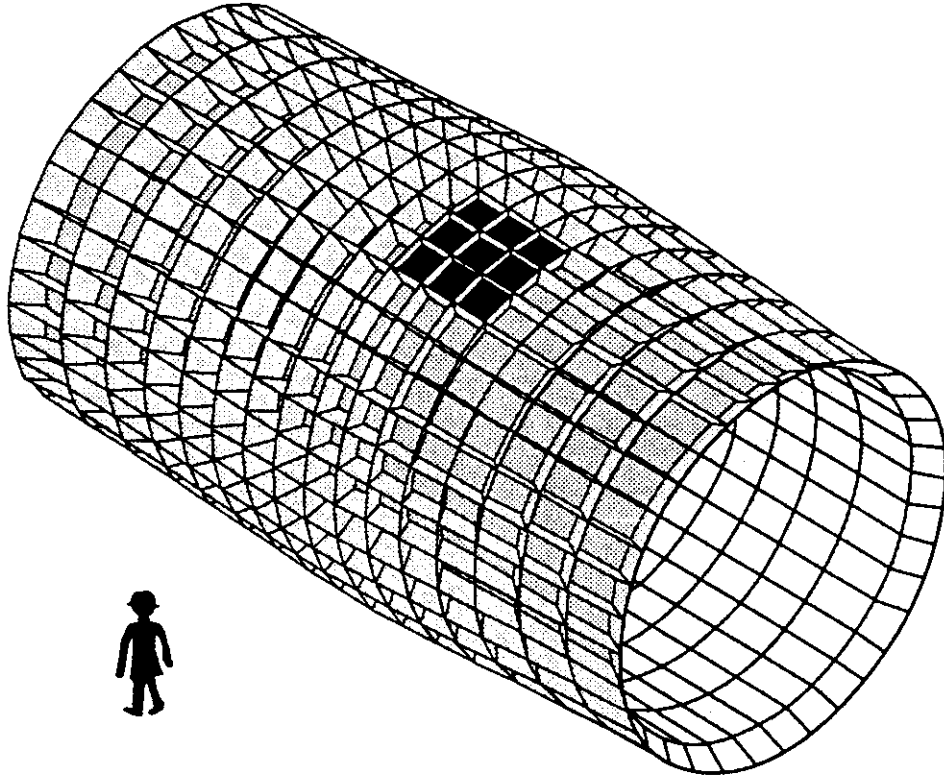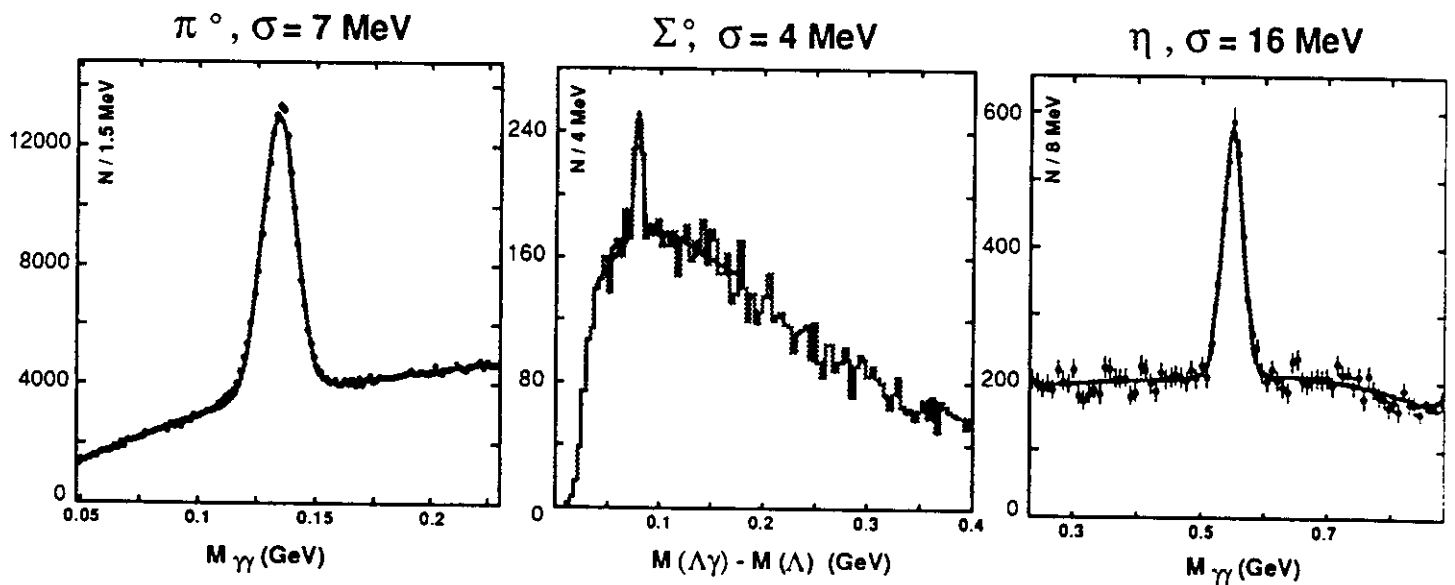cludes a cylindrical barrel (Fig. 31) of tapered, trapezoidal crystals similar to the barrel L3 BGO calorimeter, covering the interval $|\eta| \leq 1.4$. A forward endcap calorimeter covers the region $1.4 \leq |\eta| \leq 3$, and is described in section 4.10. The barrel detector has the following unique properties:

- It is located approximately 3 meters from the interaction point, so as to reduce the radiation level and neutral particle flux. Since the RMS pileup energy is inversely proportional to the calorimeter radius (Fig. 33), the pileup noise is appreciably reduced by locating the calorimeter at a large distance so that the photon density is reduced and charged particles are swept away; see Fig. 34. More details on this topic are provided in Ref. [27].

- The amount of material in front of the crystals is only 0.03 X_0.

- It measures the electromagnetic energy to better than 1 %.

- The fine granularity of the crystals eliminates the need for additional instrumentation for photon pointing (i.e. segmented crystal readout or preradiators); see Ref. [27].

- The good angular and spatial resolution of the crystal array provides a unique opportunity to study multiphoton final states, as has already been demonstrated with photons in the L3 calorimeter (Fig. 32).

4.2. Description of Detector

Several crystals [28] are good candidates for a precision electromagnetic calorimeter at LHC. For design purposes, we have assumed Cerium Fluoride (CeF_3) crystals. The crystals are located at an inner radius of ~ 3 m from the interaction point, and have a front face of approximately 3×3 cm^2 and a
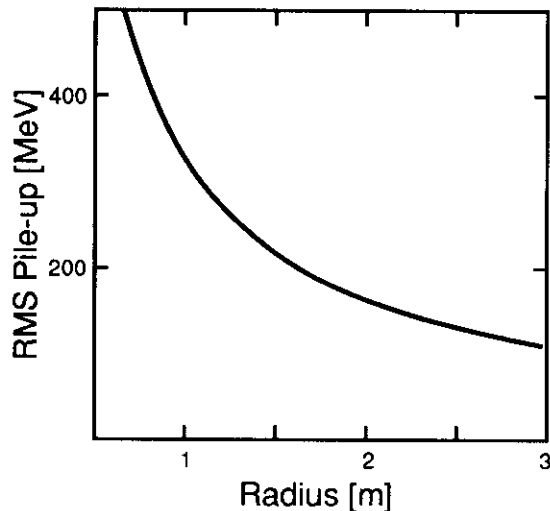
Figure 33: RMS pileup vs. radius in $\Delta\eta \times \Delta\phi \simeq 0.06 \times 0.06$ at $\mathcal{L} = 10^{34} cm^{-2} s^{-1}$ and $|\eta| \leq 1.4$ for $B = 2T$. For $B = 3T$ the RMS pileup decreases slightly with respect to the above.

length of 23 - 25 X_0. With a coverage of $|\eta| \leq 1.4$, this gives 129600 crystals (240 in η, 540 in ϕ) with $\Delta\eta \times \Delta\phi \simeq 0.01 \times 0.01$. CeF_3 properties, which have also been incorporated in the simulations, are summarized in Table 8.

Several features make CeF_3 an atractive candidate for a crystal calorimeter at LHC:

- *High Density*
  CeF_3 has a high density due to the high concentration of Ce^{3+} ions in the lattice (1.88 $\times$ $10^{22} cm^{-3}$), which yields a small radiation length and small Molière radius.

- *Fast Scintillation*
  Only crystals with optically allowed transitions (such as 5d $\rightarrow$ 4f forCe^{3+}) can give rise to a fast scintillation. The scintillation mechanism of CeF_3 is simple and well understood. It involves the fast, intense and temperature independent transition 5d $\rightarrow$ 4f of the Ce^{3+} ion. Two broad emission bands centered at 300 nm and 340 nm (see Fig. 35) produce a light yield roughly half that of BGO, and a decay time of 20 to 25 ns (see Fig. 36).

- *Good Uniformity*
  The energy resolution of the calorimeter,

Table 8: Properties of CeF_3, BGO and PbF_2

	CeF_3	BGO	PbF_2 (orthorhombic)	Units
Density	6.16	7.13	8.24	g/cm^3
Radiation Length	1.68	1.12	0.88	cm
Molière Radius	2.6	2.7	1.80	cm
Decay Time of Light	20 to 30	340	≤ 20	ns
Total Light (relative)	$\simeq 1/2$	1	a	
Emission Peak	340	480	450	nm
Temp. coeff.(at 20° C)	< 0.1	-1.4		%/° C

[a])For currently available samples (1 % orthorhombic phase), the light output is around 30 % of that of BGO. The value for final samples is expected to be better than that of BGO.
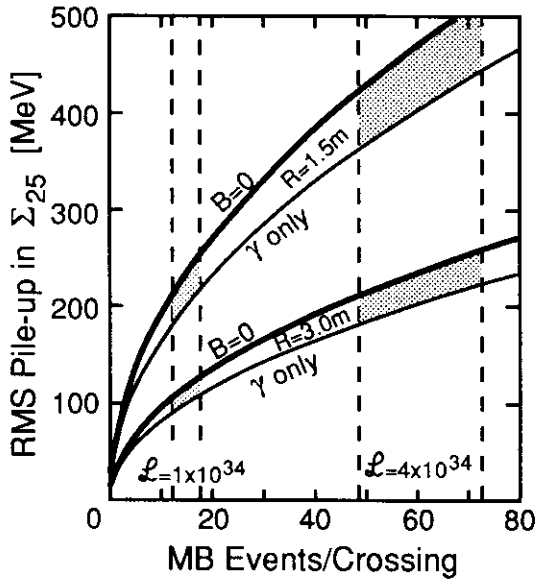

Figure 34: RMS pileup in a 5 × 5 CeF_3 crystal sum as a function of the effective number of minimum bias events per bunch crossing. The two families of curves correspond to the pileup with B = 0 and "B = ∞" (photons only) for R = 1.5 m and 3.0 m. The two vertical bands indicate the pileup at a luminosity of 1 × $10^{34}cm^{-2}sec-1$ and 4 × $10^{34}cm^{-2}sec-1$. The low value in the band is the intrinsic pileup (from physics) and the high value is for moderately fast shaping electronics (f = 1.5; f will be explained below in equation (1)). As this figure shows, the large radius L3P design is capable of very clean electron and photon detection at the highest luminosities.

and particularly the constant term, will strongly depend on all possible sources of non-uniformity. Intrinsic scintillators like CeF_3 are therefore preferred to doped materials, because it is difficult to control the uniformity of doping. The light collection in a pointing geometry will introduce a non-uniformity due to the focussing effect, which depends on the refractive index of the crystal. Cerium fluoride crystal has a refractive index around 1.62, which will limit this effect to a much smaller value than that for BGO (n=2.15). In addition, the scintillation yield from CeF_3 is almost temperature independent (less than $0.1\%/^0C$), eliminating the need for thermal insulation of the detector.

• *Radiation Hardness*

Much progress has been made recently in the radiation hardness of CeF_3 which has been shown to be intrinsically resistant up to 1,000 Gray (photons) and 10^{12} neutron/cm^2 irradiation [29]. At a distance of 3 m and $| \eta | \leq 1.4$ even with $\mathcal{L} = 4 \times 10^{34}cm^{-2}s^{-1}$ we expect a crystal lifetime exceeding 20 years. Radiation hardness depends on the quality of the raw material. In inorganic scintillators, the scintillation efficiency is generally not affected by the damage, but impurities, even in very small quantities, can create colour centres which absorb a fraction of the emitted light.

Research is in progress to find ways to identify the specific impurities which are responsible for the damage in CeF_3 and to find eco-

26
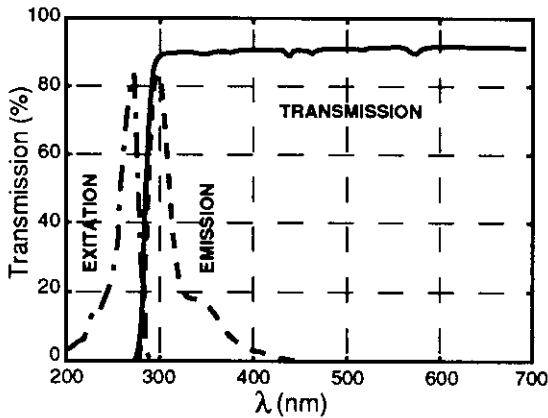
Figure 35: Transmission, Excitation and Emission Spectra of CeF$_3$
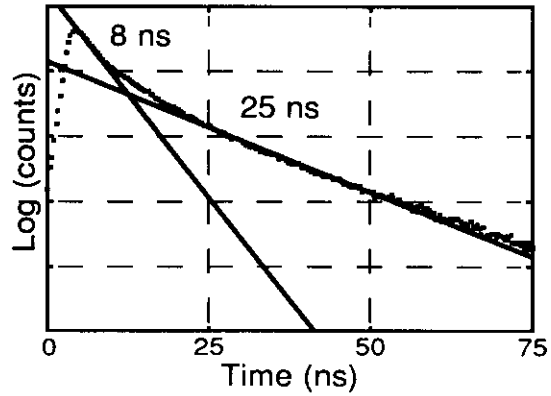
Figure 36: CeF$_3$ Decay Curve

nomical ways to remove them from the raw material.

- *Good Mechanical Properties*

  Due to the good mechanical properties of CeF$_3$, a high production yield can be expected after mechanical processing. Nonetheless, mechanical processing will be one of the dominant cost drivers, and extensive R&D is in progress to find economical techniques for cutting and polishing crystals.

- *Economical*

  Cerium is the most abundant of the rare earths, with China as the world's main producer of cerium oxide. It is widely used for several industrial applications. The preliminary results from the Crystal Clear Collaboration indicate that a purity of 99.95% is probably good enough to guarantee a good quality crystal.

  Cerium fluoride can be grown by the Bridgeman-Stockbarger technique in a graphite crucible. The high density of CeF$_3$ limits the crystal size to about 25 radiation lengths, which can be grown in furnaces of reasonable size and at modest cost.

The intrinsic EM resolution for 25 X_0 expected from a sum of 5 × 5 crystals (Σ_{25}) has been simulated with GEANT [25], and is shown in Fig. 37.

In order to keep the highest resolution, we have minimized the material in the tracker (3% X_0 to-
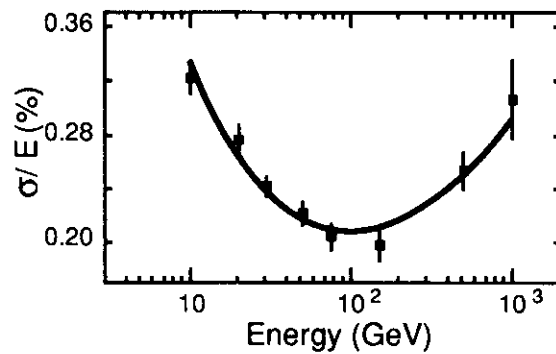
Figure 37: Intrinsic CeF$_3$ resolution for Σ_{25}.

tal), as well as the thickness of the supporting structure. This limits any degradation in resolution by supporting walls between crystals or any material before the crystals, in which showers may originate. For the purpose of calculation, the crystal resolution for a Σ_{25}, with $\frac{\sigma}{E}$ in % and E in GeV, may be parameterized as:

$$\frac{\sigma}{E} = \frac{A}{\sqrt{E}} \oplus B \oplus C \cdot E^\alpha \oplus \frac{N}{E} \oplus \frac{f \cdot \sigma_{PU}}{E} \oplus \varepsilon \quad (1)$$

where A = 0.94% is the stochastic term, B = 0.14% is the constant term, C = 0.025% and α = 0.34 represent the high energy leakage, N $\leq$ 100 MeV is the electronic noise in the $\Sigma_{25}$, σ_{PU} is the RMS pileup in the Σ_{25}, f is the electronic pileup factor, and ε is the calibration error. At a luminosity of $\mathcal{L} = 10^{34}\ cm^{-2}s^{-1}$, the resolution may thus be written as:

$$\frac{\sigma}{E} = \frac{0.94\%}{\sqrt{E}} \oplus 0.14\% \oplus 0.025\% \cdot E^{0.34} \quad (2)$$
$$\oplus \frac{10\%}{E} \oplus \frac{10\%}{E} \oplus 0.5\%$$

This formula is applicable for a low-noise vacuum photodiode readout. At high magnetic fields, where a silicon photodiode readout is required, the noise term should be replaced by $N \leq 500\ MeV$. At $\mathcal{L} = 4 \times 10^{34}cm^{-2}s^{-1}$ the resolution is only slightly affected due to the increase of the pile-up contribution (see Fig. 34).

4.3. Crystal Production in China

China has demonstrated several advantages in large-scale production of crystals: Nationwide collaboration has been organized with the strong support of the Chinese Government; infrastructure and experience to produce large quantities of crystals are already available from mass production of the L3 BGO and R&D on CeF_3, BaF_2 and PbF_2; China is a country rich in rare earth resources.

Together with ETH Zurich, a large Chinese collaboration, including research institutes, universities, and industries, exists today. The Chinese members of the collaboration and their specialties include:

- *Crystal growth:*
  Shanghai Institute of Ceramics (SIC), Shanghai. Five Bridgeman growing furnaces are in operation at SIC, as well as several cutting and polishing machines, and mechanical and optical measurement devices.

Beijing Glass Research Institute (BGRI), Beijing. Nine furnaces are in operation at BGRI, with 8 more large furnaces to be installed.

- *Mechanical processing:*
  Zhongnan Optical Instrument Factory (ZOIF), Zhicheng. ZOIF specializes in mass production of high-quality optical products, as well as machining and finishing.

- *Quality control:*
  Institute of High Energy Physics (IHEP), Beijing.

- *Study of Properties:*
  Institute of Crystal Materials, Shandong University, Jinan.
  Department of Materials Sciences and Engineering, Zhejiang University, Hangzhou.
  Tongji University, Shanghai.
  University of Sciences and Technology of China, Hefei.

The Chinese Academy of Sciences is coordinating an active R&D at all of these institutes concerning the properties of CeF_3 and the means for crystal production. We are investigating the use of raw materials with 99.95% purity by performing comparative growth experiments using CeF_3 provided by different firms, and processed from different salt materials. These studies also include composition analyses of the raw materials, as well as investigations on the pre-treatment and refining processes to be used.

Crystals of good transparency have already been successfully grown. Transmission is over 85% at 310 nm, and is still around 80% after irradiation with 1,000 Gy. Radiation hardness tests are performed on samples using a Co^{60} source, in cooperation with the Shanghai Nuclear Research Institute.

Mechanical processing is being studied with five cutting machines, two polishing machines and a large lapping machine. Results are verified with computer-controlled dimension measuring devices, and surface roughness meters. Optical properties are determined with spectrophotometers, and UV and X-ray flourescence measurements are part of the standard crystal measurements.

Rigourous quality control is required after production, before shipment and after reception of the crystals. We plan to assure quality control in a

manner similar to the L3 BGO, by performing the following steps:

- *Visual Inspection* to ensure that there are no cracks or scratches on the crystal.

- *Dimension Measurements:* Each crystal will be compared to the corresponding reference standard. The tolerance for each dimension, as compared to the standard, is +0 and -200 μm. The planarity of all six faces is 50 μm. The endfaces of the crystal are perpendicular to the two adjacent reference sidefaces to within 50 μm.

- *Transmission Measurements* will be performed by spectrophotometers.

- *Light Yield Measurements* will be performed with Cs^{137} sources. Two end points and a mid-point will be compared against a reference standard.

- *Arrival Inspection* will be performed at CERN by repeating each of these measurements.

- *Uniformity Measurements* will be performed at CERN. After the crystals have been coated, they will be measured with a cosmic ray bench, similar to what was used for the L3 BGO.

4.4. Research and Development on CeF_3, PbF_2 and $CsI(CsBr)$ Crystals

The Shanghai Institute of Ceramics(SIC) and ETH Zurich are conducting a research on new crystals for L3P (CeF_3, PbF_2 and others). The Institute of Solid State Physics, Moscow is now participating in the development of PbF_2 crystals as well.

PbF_2 is still a very attractive material worth developping, because of its low production cost and high density (see Table 8). SIC has developped a new technology to grow very clear, uniform and highly transmitting PbF_2 crystals. However, so far only Cerenkov and UV excited scintillation effects were detected on these crystals. Through the following measures, we believe, it may be possible to use these crystals in the electromagnetic calorimeter:

- Better understanding of the optical properties.

- Studies of the phase transitions of Lead Fluoride.

- Studies of doping effects.

- Improving the crystal quality to enhance the Cerenkov effect.

The Institute of Solid State Physics, Moscow, has studied the quenching mechanism of room temperature scintillation in PbF_2, and we conclude that orthorhombic PbF_2 crystals are much better scintillators than the cubic crystals normally produced. The orthorhombic phase of PbF_2 is in equilibrium at room temperature, but the phase transition from the high temperature cubic phase to the orthorhombic one does not usually take place due to the large specific volume decrease (about 10 %) from cubic to orthorhombic structure.

An application of high hydrostatic pressure does induce this transition, but due to the large internal volume contraction, a high density of microcracks appears, thus making the crystal opaque.

The specialists at the Institute of Solid State Physics, Moscow, have invented a plastic deformation procedure to initiate orthorhombic phase generation, while preserving the crystal transparency. After this deformation treatment, PbF_2 crystals grown by SIC began to scintillate at room temperature.

The decay times of PbF_2 room temperature scintillations turned out to be quite fast (less than 20 ns) with a convenient spectral range of emission (about 450 nm). The light output of the first samples was already comparable to that of CeF_3, see Table 8. The light level of this sample is limited by the small percentage of the orthorhombic phase (less than 1 %). Further experiments to increase the orthorhombic phase composition should enhance the scintillation output considerably.

Intensive R&D work is planned by the Institute of Solid State Physics, Moscow, in order to develop the scintillating PbF_2 technology on the basis of plastic deformation structural transformations. This R&D could result in the production of high density, good sensitivity, fast and cheap scintillating crystals with dimensions appropriate for L3P.

The deformation treatment technology developed by the Institute of Solid State Physics combines volume structure transformation with surface deformation flattening, which makes all of the surfaces of the crystal optically smooth. This eliminates the need for additional abrasive polishing, thus making the crystal production much more economical.

29

In addition, the Physics Institute of the University of Tbilisi, Georgia and the Institute for Mono Crystals in Kharkov, Ukrainia are studying CsI(CsBr) crystals in collaboration with the Paul Scherrer Institute (PSI), Switzerland.

Czechoslovakia has expertise in the production of heavy crystal scintillators, laser crystals and heavy glasses doped with rare elements. The collaborating institutes include the Preciosa/Monokrystaly (former Crystur) Company in Turnov, the Tesla Company, Research Institute of Nuclear Instrumentation, in Premysleni and the State Research Institute of Glass in Hradec Kralove (for more details see [27]).

4.5. Readout

Electromagnetic calorimeter readout at high-luminosity hadron colliders presents unprecedented challenges in signal acquisition. The dynamic range requirements equal or exceed those at LEP, with three orders of magnitude increase in speed going from LEP to LHC. In addition, the extremely high bunch crossing frequency necessitates a "pipelined" readout: Because the time between successive interactions is much less than the time needed to form a trigger decision, the information (energy deposited in the calorimeter) associated with a given bunch crossing must be stored in some fashion for several (tens to hundreds) of bunches before a trigger decision is available. The combination of these factors, with the requirement for high resolution, demands considerable attention at each stage of the readout.

Operation of the detector in a magnetic field places limitations on the choice of a photodetector. There are several candidate photodevices (avalanche photodiodes, hybrid photodiodes, silicon photodiodes, vacuum photodetectors, etc.) each with advantages as well as disadvantages. Large-area silicon photodiodes have successfully been used as photodetectors for calorimeters operating in the μs timing regime. The largest such system with silicon photodiodes is the L3 BGO electromagnetic calorimeter [15], whose performance specifications are listed in Table 9.

The noise performance of a silicon photodiode system at the LHC may then be roughly estimated as follows: For a single-component scintillator (like BGO or CeF_3), the photocurrent is proportional to $(Q/\tau)e^{-t/\tau}$, where Q is the number of photoelectrons/MeV and τ is the decay time constant of the light. If all of the charge can be integrated in

a single bunch crossing (as is the case with BGO at LEP), then the available signal is simply proportional to Q. At the LHC, however, one would need some 5 to 10 bunch crossings to collect most of the CeF_3 charge, so that the signal available is proportional to $Q \cdot (\tau_S/\tau)$, where τ_S is the effective electronic shaping time of the signal (for a linear system). As the noise for a given preamplifier is proportional to $C \cdot \tau_S^{-1/2}$, where C is the total capacitance at the input of the preamplifier, the Signal-to-Noise ratio at LHC behaves like

$$\frac{S}{N} \sim \left(\frac{Q}{C}\right) \cdot \frac{\tau_S^{3/2}}{\tau} \qquad (3)$$

so that as the shaping time τ_S is made shorter, the S/N ratio degrades as $\tau_S^{3/2}$.

In going from L3 BGO (LEP) to L3P CeF_3 (LHC), 1 MeV of noise at LEP will become more than 100 MeV of noise at LHC. Although there now exist large area silicon photodiodes with thicker depletion layers than those used on the BGO (thus with somewhat lower capacitance per cm^2, but with increased leakage current and susceptibility to radiation damage) such diodes with fast shaping amplifiers would still produce at least 75 to 100 MeV of noise per crystal.

Vacuum photodiodes, which have lower leakage current and faster risetime, have a noise performance which is an order of magnitude superior to silicon photodiodes. Further, the only radiation hardness problem with a vacuum device is the envelope, whereas silicon photodiodes exhibit gain changes, leakage current increases and reduced lifetimes in radiation environments. Although additional gain is possible (phototriode, tetrode, ...) for maximum gain stability and ease of operation in a magnetic field, a photodiode is the favored solution.

Operating a vacuum photodevice in a strong magnetic field requires orienting the tube axis (the electric field axis) with some angle less than 90 degrees with respect to the magnetic field axis. A proximity focussed photodiode can easily operate at moderate fields with only a small tilt angle, and no appreciable gain loss (so that the gain as a function of η is constant). Such a tilt angle has only a small effect on the light collection and mechanics. A higher gain device, while providing more signal, requires a much greater tilt angle, and operates with reduced gain in the field. As the magnetic field grows stronger, however, it becomes increas-

Table 9: L3 BGO Readout

Crystal Back Face	$9\ cm^2$
Readout	$3\ cm^2$ Si photodiode
Capacitance	$75\ pF/cm^2 + 75\ pF$ Preamp
Effective Dynamic Range	> 18 bits (< 1 MeV to 250 GeV)
Intrinsic Noise	0.8 MeV ($\simeq 900$ electrons RMS)
Total Noise	1 MeV
Residual on next bunch	$< 10^{-5}$

ingly impractical to employ vaccuum photodiodes, thus another readout scheme, such as using silicon photodiodes, must be developed (although attaining the required noise performance with silicon photodiodes will require considerable R&D).

The electronic readout chain consists of photodiodes with preamplifiers, shaping and gain stages, signal acquisition, and the higher level readout and trigger stages. The crystals that form a trigger tower (a 5 × 5 array of crystals) comprise a conceptual readout module, and share common electrical services. The preamplifiers are located directly behind (or on) the photodetectors, and have short cable runs to shaping and line driving stages. Because of the high dynamic range and large bandwidth, the signals are split into two components (a high and low gain channel) directly at the shaping stage, before proceeding to the signal acquisition electronics.

The data pipeline may be formed either in an analog fashion, in which case the pipeline consists of a switched capacitor array with virtual 1st and 2nd level memories formed by pointers; or in a digital fashion, with high speed ADCs and digital 1st and 2nd level memories. Because of the comparative ease in forming a 1st level trigger, as well as the higher fidelity of digitization, we favor the digital pipeline approach.

With the digital pipeline, the multiple range signals are digitized either by separate ADCs, or multiplexed into a single ADC. The resulting data, an ADC mantissa, along with identification bits indicating which range was used, are then stored in digital memory awaiting trigger decisions. The same data are then presented to a lookup table (RAM) whose outputs correspond to a calibrated energy (or transverse energy) to be used in the trigger decision. The trigger may be formed either as an analog current sum, in which case the calibrated digital data drive a fast current-output DAC; or in

a digital fashion with a pipelined adder. Note that the analog sum formed from digital data differs markedly from an analog sum formed by adding shaped copies of the raw input signal in that the data are already calibrated, the effects of time slewing have been completely eliminated, and the bandwidth is considerably reduced, so that the resulting signal is much cleaner and more precise than would be possible with a classical analog sum.

Noise level estimates for the crystal readout have been presented in [27]. An additional problem arises at high luminosity because the time between bunches at LHC is short compared to the time needed to integrate the full detector charge. The electronic enhancement of pileup must therefore be included in the overall detector resolution. For a linear shaping system with voltage sampling, if a_i represents the normalized gain (the height of the pulse on the ith bunch after "t = 0", normalized to the peak height) then the increase in the observed pileup due to the tails of pileup pulses from previous bunches is given by $\sigma_{OBS} = f \cdot \sigma_{PU}$, where $f^2 = \Sigma a_i^2$ is the electronic pileup factor ($f \geq 1$).

4.6. Trigger

The designs that are currently favored for calorimetric triggering at high-luminosity hadron colliders consist of multi-level trigger stages, each stage performing more powerful analysis on the data. The first stage trigger is generally a fully hardware trigger processor which operates on special trigger data constructed by the Level 1 readout. The final stage is a fully software trigger processor operating on the main readout data, and the intermediate stage may operate either on the trigger data or the main readout data.

With such a design, severe requirements are placed on the Level 1 trigger, which must return a trigger decision within a few μs, while accepting input data every 15 ns. Such a Level 1 trigger

31

Table 10: Calorimetric Trigger

Level	Description	Timing
Level 0:	Synchronous Hardware processor	$\ll 1 \ \mu s$
	Local computation of hits above thresholds	
Level 1:	Synchronous or Monotonic Hardware processor	$10 - 100 \ \mu s$
	Crude Isolation cut and matching with HCAL towers	
Level 2:	Monotonic Software processor	> 1 ms
	Precise Isolation cut	
	Charged Energy cut (with tracker)	
Level 3:	Software processors	
	"Off line" analysis	

must therefore be pipelined (each operation of the trigger is clocked by the beam clock) so that the processing capability of Level 1 is highly restricted. To overcome this problem, our calorimetric trigger adds an additional stage, Level 0, which performs simple, local discrimination. The addition of this level, simplifies construction of the trigger, and allows one to two orders of magnitude more computation time for Level 1. The organization and functionality of the trigger stages are described in Table 10. The basic trigger flow is then as follows. An energy sum, as well as a few bits corresponding to hits above threshold are formed for each electromagnetic trigger tower. Level 0 receives the trigger bits, and forms a trigger decision based on n hits above threshold (n_1 hits above E_1, n_2 hits above E_2, etc.). If the Level 0 decision is yes, then the digitized 1st level data are stored in the local 1st level memory while Level 1 processes the trigger tower-sum data. A Level 1 yes causes the data in the 1st level memory to be loaded into the 2nd level buffer, for readout to the Level 2 trigger.

Extensive simulation has been performed to ascertain the trigger rates in the electromagnetic calorimeter and verify the performance of trigger cuts; see Ref. [27].

4.7. Calibration

Experience with the L3 BGO calorimeter shows that several design parameters must be carefully chosen to optimize resolution and calibration stability. Whereas the BGO was designed to have optimum resolution at low energies, the CeF_3 calorimeter should have optimum resolution at high energies. Some of the relevant design parameters are listed in Table 11.

Each of these effects has a major contribution

to calibration stability. Temperature effects, while important for BGO, are expected to be very small in CeF_3. The nonuniformities and nonlinearities due to geometry, reflectors, index of refraction and attenuation length are less critical in CeF_3 than BGO. The choice of calibration energies is also important, because the errors due to nonlinearities depend on the ratio of the energy being measured to the nearest calibration energy. For example, a simple gain error, such as mismeasuring the gain of a crystal channel i by some amount ε_i introduces a constant term of $c = RMS(\varepsilon_i)$ in the energy resolution.

A nonlinearity, $E_{MEAS} = \alpha_i E + \beta_i E^2$ introduces a constant term of $c = RMS(\alpha_i) \cdot (1 - E/E_{CAL})$, which then depends on the difference between E and E_{CAL}.

The initial calibration and detailed understanding of the crystal nonlinearities requires excellent incident momentum and position definition, together with fairly high statistics. As with the L3 BGO, this initial calibration will be performed in a test beam. The crystal ring assemblies (described below) are mounted on a rotating table, so that each crystal may be positioned on the test beam axis. In one 14 second SPS cycle, the two second beam burst contains a sufficient number of particles to calibrate the crystal. In the remaining 12 seconds, the turntable moves to the next crystal so that <15 seconds per crystal are required for calibration.

After installation, we will perform in situ calibration monitoring, in order to make small corrections to the initial calibration constants for any gain drifts. This calibration monitoring will be done with isolated $e^{\pm}$ from W, $Z \rightarrow e^{\pm} + X$ (in $|\eta| \leq 1.4$,

Table 11: Calibration Stability - CeF_3 vs. BGO

Effect	BGO	CeF3
Temp. coeff.	-1.4 %/°C	< 0.1%/°C
Geometry	R = 55 cm	R = 290 cm (Angles are smaller)
Uniformity	Wide range used Optimized low energy	Small range must be used, and optimized for high energy
Index of refraction	High	Low, better uniformity
Calibration Energy	One, 10 GeV	Several, high E
High energy in situ calibration possible	No	Yes

more than 90% of the $e^{\pm}$ are isolated). The calibration monitoring makes use of E/p matching with the tracker, followed by resolution optimization. (This technique is possible because the original calibration constants are already known. Such a technique is insufficient for actual calibration ab initio.) With the high resolution of the tracker, $\delta p/p = 1\%$ at $p_T = 100\ GeV$, the number of events required to monitor the calibration to an accuracy of ε is given by

$$N = \left(\left(\frac{\delta E}{E} \right)^2 + \left(\frac{\delta p}{p} \right)^2 + \left(\frac{\sigma_{PU}}{E} \right)^2 + \left(\frac{\sigma_N}{E} \right)^2 \right) / \varepsilon^2,$$

(4)

where $\delta E/E$ is the crystal resolution ($\delta E/E \simeq$ 0.5% for Σ_{25} and $\delta E/E \simeq 1\%$ for Σ_9), σ_{PU} is the RMS pileup at the luminosity where the calibration is being monitored, and σ_N is the electronics noise. To monitor the calibration to an accuracy of $\varepsilon = 0.3\%$ at 50 GeV thus requires at least 10 events/crystal. The cross-section for isolated $e^{\pm}$ from W, $Z \to e^{\pm} + X$ in $|\eta| \leq 1.4$ is about 7 nb for $p_T > 30$ GeV and about 850 pb for $p_T = 50 \pm 6$ GeV. Calibration monitoring to an accuracy of $\varepsilon = 0.3\%$ at $E = 50 \pm 6$ GeV can therefore be performed over the entire detector on the order of 6 times per year (10^7 s) at $\mathcal{L} = 10^{33}\ cm^{-2}s^{-1}$ and 65 times per year at $\mathcal{L} = 10^{34}\ cm^{-2}s^{-1}$.

Additional gain monitoring systems, such as light pulsers or electronic test pulses may be employed. Several experiments have used light pulsers to monitor gain stability, however the problems that will arise at LHC speeds, due to the vast difference in the light pulse shape and the scintillation pulse shape, may be non-trivial to solve. Electronic test pulsing may be readily performed with the addition of local test pulse drivers on each channel,

however with proper electronic design, electronic gain drift should not pose a serious problem (the 12,000 channel L3 BGO Level 1 readout has maintained electronic gain stability of better than 0.01% over 5 years of operation).

4.8. Mechanical Support

The crystal electromagnetic calorimeter is detailed in Ref. [27], and consists of an array of crystals with pyramidal frustum shapes pointing to the interaction point. It is divided into 540 identical ϕ slices and each slice contains 240 crystals with mirror symmetry. The total crystal volume is about 64 m^3 and the corresponding weight is 400 tons.

A very rigid supporting structure is needed to take this load with tolerable deformations. As crystals cannot take any part of the deformations, clearance between crystals must be foreseen and a compromise found between incurred solid angle loss and exceeding dimensions of the supporting structure. From the experience gained in L3 during the construction of the BGO calorimeter, a similar principle is used to minimize solid angular loss: structural material is optimized for the rigidity and resistance needed once in place in the experiment. Reinforcements are used during assembly and installation maneuvers to compensate the progressive loading during assembly, the position changes during transportation, calibration and installation maneuvers, and occasional accelerations due to shocks.

Each crystal has a constant front area of 1150 mm^2, and a height of 390 mm. For reasons of economy in the processing of the crystals, the front face and two side faces are made perpendicular to each other to define a reference trihedron (Fig. 38). There are therefore 120 different crystal shapes
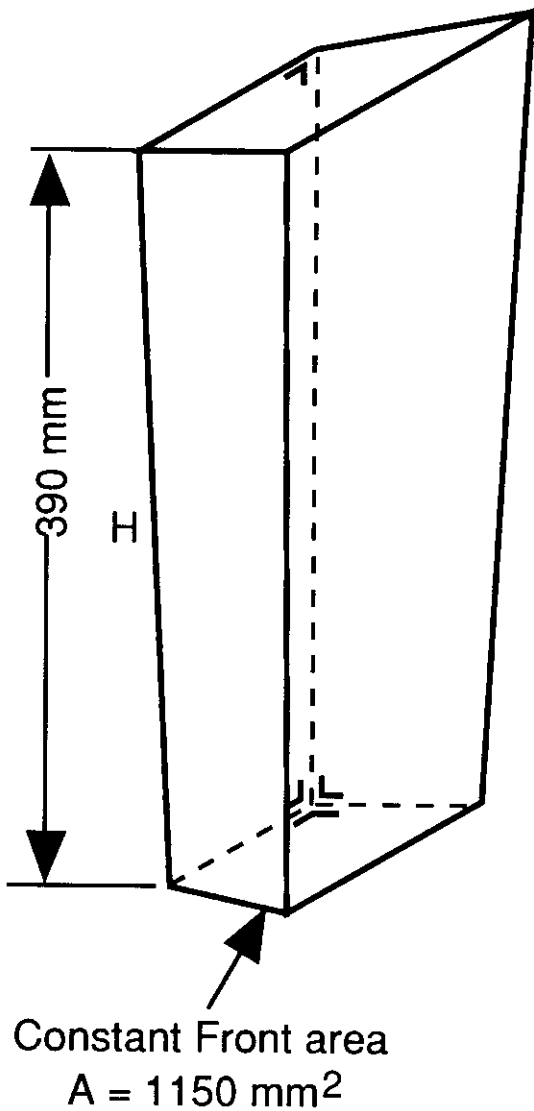
33

Figure 39: Photodiode and capsule
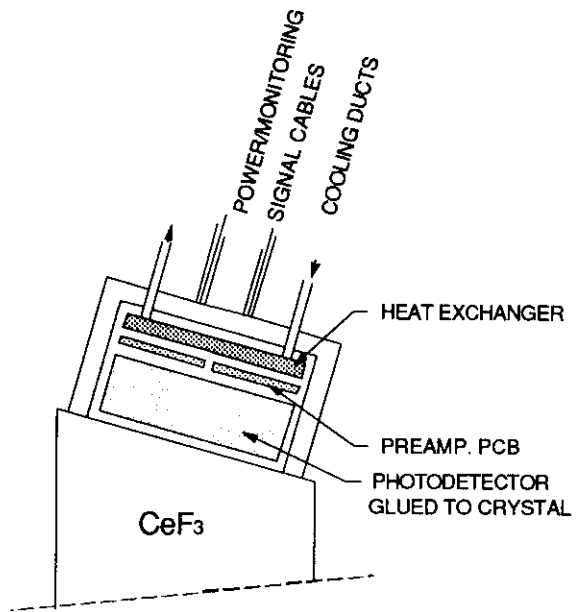

Constant Front area

A = 1150 mm²

Figure 38: Crystal geometry

(right hand) and their 120 symmetrical counterparts (left hand).

As with the L3 BGO calorimeter, every crystal is equipped with a photodetector located on its back face with a glued coolant-, gas- and light- tight plastic capsule. The capsule contains:

- The photodetector, which is glued with a special adhesive to the back face of the crystal.

- A preamplifier board.

- Cables for power supply, readout and control.

- Cooling ducts connected to a small metal heat exchanger in good thermal contact with the preamplifier board.

The capsule is rigid enough to transmit the force setting the crystal into correct position and to evenly share it on the crystal back face to avoid dangerous stress concentrations (Fig. 39).

The electromagnetic calorimeter is divided into 16 rings of 8 different shapes. Rings are two-by-two mirror-symmetric. Each ring is made of 36 modular identical crates.

One crate contains 15 crystals in ϕ and 15 crystals in η. A crate with its 225 crystals weighs
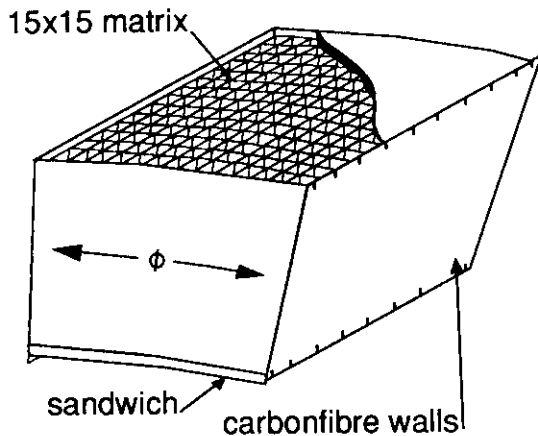
34

Figure 40: Crystal crates

about 700 kg (see Fig. 40). Each crate is a box with 5mm thick metallised carbon fibre composite or 2mm thick titanium alloy side walls, with parallel faces in ϕ and tapered faces in η. With this design the solid angle loss due to material is 0.3 %.

There is no structural partitioning wall between each crystal. The bottom of the crate is a light sandwich panel. Crystals are held in position by a frame which closes the back of the crate. The frame carries pressing devices pushing on the crystal capsules so that crystals are accurately set on the corresponding step-like bottom face of the crate.

Some freedom is necessary between crystals after the optical separation film is inserted, because of the combined dimensional tolerances of the crate and crystals, and to allow for expected elastic deformation of the crate during handling operations. The 225 individual forces applied on the crate bottom are reacted by an equivalent 13.5 kN tension in the side walls, which enhances their rigidity so that assembled crates are self-supporting in any position.

4.9. Assembly, Installation and Calibration Mechanics
4.9.1. Calorimeter Assembly

The calorimeter consists of modular rings, which facilitate the assembly at each stage. For crystal loading, the open crate is set inside an assembly container with very rigid walls so that it is undeformed during insertion of the 700 kg of crystals. Once the 225 crystals are installed, preamplifiers

and their cooling devices are connected, and complete tests are performed to check circuit continuity, insulation and tightness. The closing frame is fastened to the side walls and mechanical pressure is applied on the back of the crystal. This procedure was successfully used for the assembly of the BGO crystals in the L3 endcap modules.

Before lowering into the experiment, the calorimeter is pre-assembled in 16 rings on the surface. 36 crates are assembled horizontally in a ring on a circular jig. These rings weigh about 25 tons without jig weight. Once assembled and tensioned, the ring assembly is rotated to the vertical position, then lowered to the pit with the existing 63 ton crane.

4.9.2. Calorimeter Beam Calibration Mechanics

Once rings are assembled, they are ready for beam calibration. The jig is fit for mounting on a rotary table providing the ϕ orientation and the η inclination (see Fig. 41). The cable and service connections do not allow a complete 2π rotation in ϕ during a calibration run. It is realistic to foresee calibration of the 15 η layers of crystals on 270 ϕ positions in one run, then a 180 degree rotation of the assembly including the cables and services attached, and a second run for the remaining half ring. As described above, the two second extracted beam burst is used to calibrate one crystal, after which the table is rotated to the position of the next crystal during the remaining 12 seconds of the SPS cycle. The active calibration time (27 hours per ring) is small compared to the total setup time.

4.9.3. Calorimeter Installation

The calorimeter is suspended inside of a support tube (ST), which is 13 meters in length, has an inner radius of 3,390 mm, and an outer radius of 3,490 mm. Its design details are given in Ref. [27]. After the support tube is in place, the rings may be installed. In order to balance the pre-stresses which give the calorimeter its stability in spite of its very light structure, the rings must be installed in symmetric pairs, starting with the central ones. This implies that access is required simultaneously from both sides of the detector (see Fig. 42).

Two railways are installed on both sides of the detector and are continued inside the support-tube using the available fixation points. The ring-jigs are attached to carriages rolling on the railway. The carriages are counterweighted to cantilever the ring
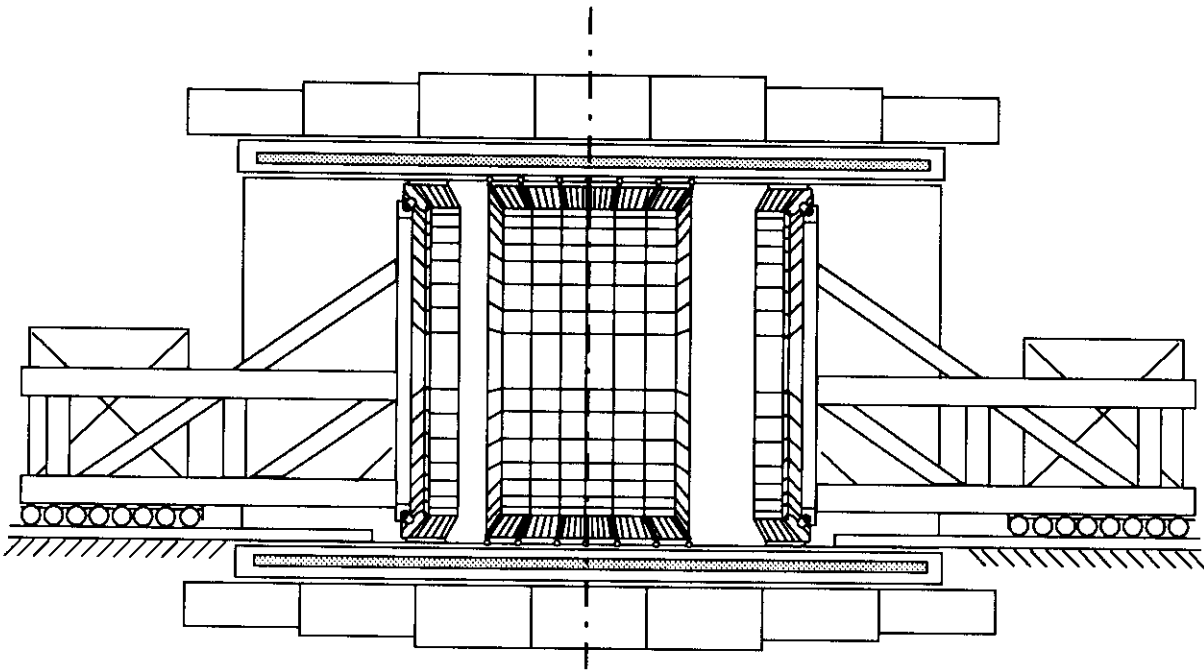
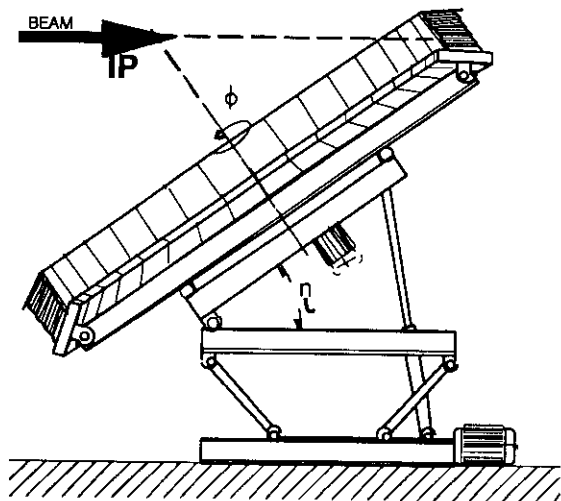Figure 42: Installation of rings in the support tube

Figure 41: Beam calibration set up

load. For each pair of rings to be installed, the rails inside the support-tube are withdrawn to leave the ring length free.

When the two rings are in position they are attached together and spokes are connected to the fixation points of the support-tube. Spokes are tensioned, and expected deformations must be monitored until the jigs can be detached from the rings. The spoke positions on the ring circumference are scattered from one ring to the next so that rings can be temporily fastened both to the jigs and to the spokes.

The computed support tube deformations are such that there will be no need to readjust the spoke tensions of previously installed rings after a ring pair is added. The spoke tensioning device can therefore be made simple, as no remote action will be required.

4.10. Endcap Electromagnetic Calorimeter

The endcap electromagnetic calorimeter, which covers the range $1.4 \leq |\eta| \leq 3.0$, consists of a high granularity silicon calorimeter (see Figs. 43, 44, 45). The energy resolution for this calorimeter is $\sim 20\%/\sqrt{E} \oplus 2\%$, which is appropriate

36

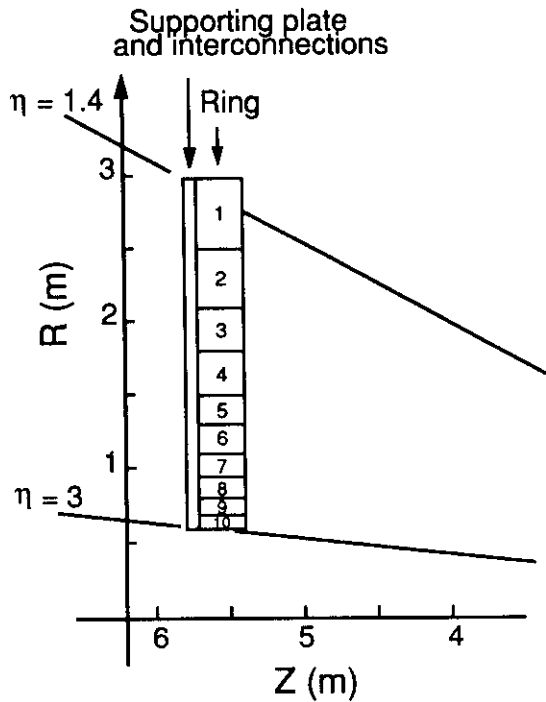## Supporting plate and interconnections

Figure 43: Schematic view of the endcap silicon calorimeter layout
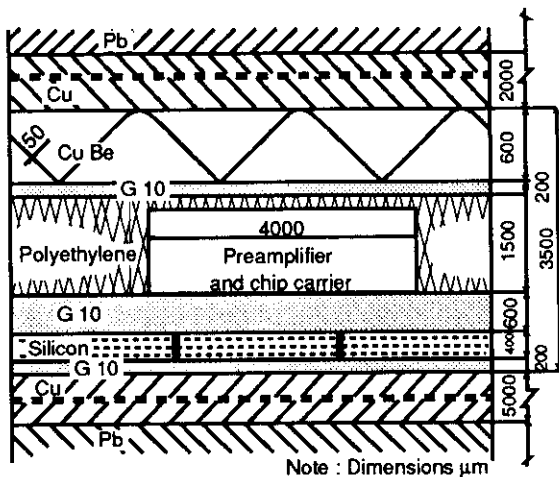

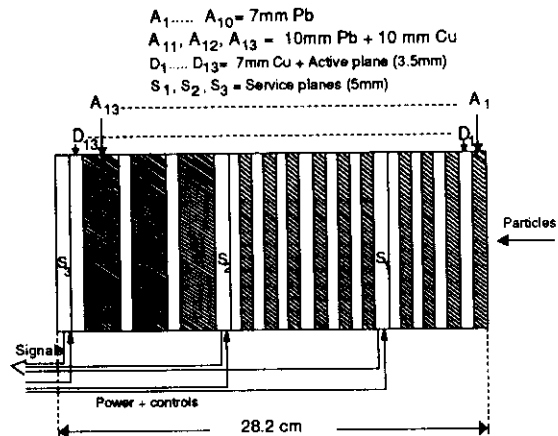Figure 44: Cross section of an active plane showing the preamplifier

Figure 45: Cross-section of the calorimeter

for the reaction H → 4e.

The design of the calorimeter is based on the experience gained by the SICAPO [17] collaboration, and on the R&D proposal P34 [32] which is developping low-cost silicon production and constructing a full scale calorimeter module.

The calorimeter consists of 13 sampling layers. The first 10 layers are 1.5 X_0 thick and the last three are 3.0 X_0. The total calorimeter depth is 24.0 X_0.

The mechanical structure is divided up into 10 rings supported at the back by a thick plate. All external connections are routed along this plate as shown in Fig. 43.

Each ring is subdivided in $\Delta\phi$ sectors, and covers $\Delta\eta = 0.15 - 0.2$.

Silicon detectors planes (active planes) are located between copper and lead absorbers. They consist of silicon diodes 400 μm thick, with an active area of 2×2 cm^2, matching the Molière radius of the calorimeter ($\rho_M = 1.8$ cm). The diodes are sandwiched between two printed circuit boards. One board contains the preamplifiers lodged in holes in a sheet of polyethylene envisaged to moderate neutrons. The second board carries the high voltage. The entire sampling layer is covered by a third board for mechanical protection, and enclosed in a copper box. A spring made of Cu-Be foil adapts the 3.0 mm thick active plane to the 3.5 mm free space inside the box. The detailed structure is shown in Fig. 44.

The rest of the absorber is Pb, 7 mm thick in

37

Table 12: Main parameters of the silicon calorimeter

η coverage	1.4 - 3.0
Total depth	24 X_0
Total geometrical thickness	28.2 cm
Sampling layers	13
Smallest cell size	2×2 cm^2
Largest cell size	4×4 cm^2
Total Si surface area	690 m^2
Number of silicon diodes	$1.7 \cdot 10^6$
Number of preamplifier channels	600K
Number of summing channels	150K
Number of readout channels	90K
Cu weight	58 t
Pb weight	61 t

Figure 46: Distribution of leakage current of fully depleted detectors produced by ELMA

the first 10 layers to complement the Cu absorber to 1.5 X_0, and 10 mm thick in the last 3 layers to complement the 7 mm Cu and the mechanical supporting structure (10 mm/layer). The total thickness of the calorimeter is thus 28.2 cm, including the space for the 3 service planes described below (see Fig. 45).

The Si diodes are readout by preamplifiers whose outputs are summed to form minitowers and buffered in an analog pipeline memory before being sent outside for further processing. The charge sensitive preamplifiers are based on the design developed by the SICAPO collaboration and adapted for the readout in the P34 R&D proposal. They are very fast (shaping time = 20 ns) and can match the Pipeline Analog Memories developed at CERN [33]. Four preamp channels are contained in a VLSI chip. They dissipate 45 mW/channel with a dynamic range of 10^5. Hence the power dissipated on the active plane never exceeds 110 W/m^2.

The copper plates act as heat conducting sheets, allowing heat exchange to the cooling circuit. A model simulation shows that the temperature gradients are less than 2° C with an average value of 10° C. This temperature is necessary to mantain a low leakage current after irradiation.

The 13 active planes are longitudinally organized in 3 segments of 4, 6, and 3 layers. At the end of each longitudinal segment, the gap between the absorbers is increased to allow a service plane carrying the HV distribution to the planes of the segment, the summing of the signals from the planes of the
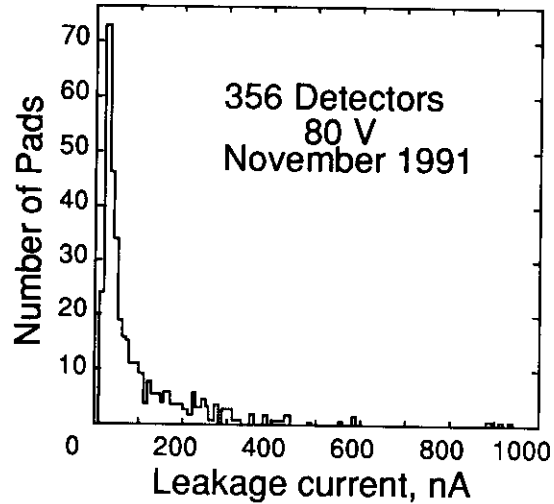
segment to form projective minitowers, the pipelining of their outputs, the controls and the protection devices. With this organization, the number of interconnections is minimized (bonding only), thus reducing the electronics costs. To reduce the number of readout channels further in the region $\eta =$ 1.4 to $\eta = 2.2$, 4 adjacent silicon diodes will be summed up.

Taking into account the moderation effect of the polyethylene located in the active samplers (see Fig. 44), in 10 years of operation the estimated neutron fluence will be less than $5 \times 10^{13} n/cm^2$ down to $\eta = 2.5$. This fluence increases gradually to $2 \times 10^{13} n/cm^2$ in one year at $\eta = 3.0$. Radiation damage may therefore require replacement of some of the silicon (up to 20 m^2) after 5 to 10 years of full intensity and continous running.

The silicon could be supplied by Russian Industry. The first lot of detectors produced last year in the framework of an extensive R&D program, demonstrated sufficiently good characteristics (see Fig. 46) for the leakage current distribution.

This R&D program includes extensive radiation damage tests, the study of the organization of a silicon system to be used in calorimetry and the preparation of a full scale subsystem prototype [32].

The main parameters of the endcap silicon calorimeter (for both endcaps) are summarized in Table 12.

4.11. Conclusions

The key features of our design may be summarized as follows:

- *Availability of Crystals:* A coordinated national effort is under way in China, with the intent of providing us with the large quantities of crystals needed at the minimum price. Such efforts have already been proven successful with the 12,000 crystal L3 BGO calorimeter.

- *Large Radius:* Background is inherently lower as the detector is located farther away from the interaction point, pileup noise and front-end trigger rates are reduced and the π^0 rejection is enhanced. A large-radius design ensures the least sensitivity to errors in the present assumptions of the backgrounds and ensures the best physics performance at any LHC luminosity.

- *Simplicity:* The performance of our barrel calorimeter is achieved solely through the use of crystals, without reliance on complex photon pointing or π^0 detector systems. Avoiding split crystals for additional detectors eases the task of maintaining precision calibration.

- *The design is based on proven L3 experience.*

39